Journal of Drug Delivery Science and Technology 89 (2023) 105072

Contents lists available at ScienceDirect

Journal of Drug Delivery Science and Technology

journal homepage: www.elsevier.com/locate/jddst

The ZnO-based fibrous poly(L-lactide-co-glycolide)/gelatin dressings enable rapid hemostasis and skin regeneration in an infectious wound model

Zhengchao Yuan [a,1], Lixiang Zhang [b,1], Hui Zheng [c,1], Muhammad Shafiq [d], Jiahui Song [a], BinBin Sun [a], Mohamed EL-Newehy [e], Hany EL-Hamshary [e], Yosry Morsi [f], Chao Huang [g,**], Xiumei Mo [a,***], Yuan Xu [b,*]

[a] State Key Laboratory for Modification of Chemical Fibers and Polymer Materials, Shanghai Engineering Research Center of Nano-Biomaterials and Regenerative Medicine, College of Chemistry, Chemical Engineering and Biotechnology, Donghua University, Shanghai, 201620, PR China
[b] Department of Orthopaedics, Xinqiao Hospital, Army Military Medical University, No. 183, Xinqiao Street, Shapingba District, Chongqing, 400037, PR China
[c] Department of Thoracic Surgery, Shanghai Pulmonary Hospital, Tongji University School of Medicine, Shanghai, 200443, PR China
[d] Innovation Center of Nanomedicine, Kawasaki Institute of Industrial Promotion, Kawasaki, Kanagawa, 210-0821, Japan
[e] Department of Chemistry, College of Science, King Saud University, P.O. Box 2455, Riyadh, 11451, Saudi Arabia
[f] Faculty of Engineering and Industrial Sciences, Swinburne University of Technology, Boroondara, VIC, 3122, Australia
[g] Shanghai Haohai Biological Technology Co., Ltd, Shanghai, 200336, PR China

ARTICLE INFO

Keywords:
Electrospinning
Nanofiber membrane
Wound healing
Zinc oxide
Hemostatic
Skin

ABSTRACT

Bacterial infections and poor hemostasis delay infectious wound healing, which require alternative strategies for functional skin repair. Zinc oxide nanoparticles (ZnO NPs) have been shown to exert the rapid hemostasis and a potent antibacterial effect against Gram-positive and Gram-negative bacterial species. The objective of this research was to explore beneficial effect of ZnO NPs-encapsulated poly(L-lactide-co-glycolide)/gelatin membranes for infectious wound healing. Electrospun membranes containing ZnO NPs exhibited good cytocompatibility and hemostatic effect *in vitro*. The membranes containing ZnO NPs also exhibited good antibacterial effect against Staphylococcus aureus (*S.* aureus) and Escherichia coli (*E.* coli) bacterial species *in vitro* alongside inducing rapid hemostasis in a rat tail-amputation model and an ear artery injury model in rabbits *in vivo*. Moreover, membranes containing ZnO NPs also induced rapid wound regeneration of *S. aureus*-infected full-thickness excisional defects in rats as manifested by the significant reduction in the wound area as well as the formation of scar-like tissues than that of the untreated (control), biocellulose-based dressings (positive control), and membranes devoid of ZnO NPs. Taken together, electrospun membranes containing ZnO may be beneficial for infectious wound healing.

Authors' statement

Zhengchao Yuan, Lixiang Zhang, Hui Zheng, Muhammad Shafiq, Jiahui Song: Conceptualization, Methodology, Writing-Original draft preparation; Zhengchao Yuan, Muhammad Shafiq, Binbin Sun; Lixiang Zhang: Writing- Reviewing and Editing; Mohamed EL-Newehy, Hany EL-Hamshary, Yosry Morsi: Writing- Reviewing and Editing; Xiumei Mo, Yuan Xu; Muhammad Shafiq, Zhengchao Yuan, Hui Zheng: Writing-Reviewing and Editing; Funding Acquisition; Supervision; Validation, Formal analysis, Investigation, Resource Data Curation and Visualization.

1. Introduction

Skin is the largest part of the body and the first line of the defense to different types of toxins and pathogens [1]. However, skin tissues are often damaged for up to varying degrees by a myriad of factors, including bacterial infections, large-scale wounds, burns, and chronic

* Corresponding author.
** Corresponding author.
*** Corresponding author.
E-mail addresses: joehuang@3healthcare.com (C. Huang), xmm@dhu.edu.cn (X. Mo), 15123161526@163.com (Y. Xu).
[1] These authors contributed equally to this work.

https://doi.org/10.1016/j.jddst.2023.105072
Received 24 May 2023; Received in revised form 6 October 2023; Accepted 14 October 2023
Available online 21 October 2023
1773-2247/

non-healing ulcers [2]. Moreover, infectious wounds may become tedious to be healed [3]. The normal wound healing is a dynamic and an interactive process, which is divided into several sequential overlapping phases, such as hemostasis, inflammation, re-epithelialization, and resolution/tissue remodeling. These wound healing stages require a cooperative effect of various types of bioactive cues, cell types (e.g., fibroblasts, endothelial cells (ECs), keratinocytes, epithelial cells, etc.) and extracellular matrix (ECM) components [4]. Chronic non-healing wounds, including infectious wounds and diabetic foot ulcers are often plagued by the poor healing presumably due to an aberrant regulation of one or more complex molecular and biological events [5]. Especially, infectious non-healing skin wounds may also perturb above-mentioned healing stages presumably due to an abnormal consumption of nutrients, limited mobilization and recruitment of endogenous stem/progenitor cells, and an excessive inflammatory response [6].

While the key aspects leading to the poor healing of infectious wounds are yet to be unveiled, it is generally considered that vascular dysfunctions and the sacracity of ECs may lead to an insufficient oxygenation and fewer nutrients in wounds, which may further exacerbate the production of reactive oxygen species (ROS) [7]. Moreover, biofilm-producing bacterial colonies may also accelerate and aggravate the pathology of the different types of wounds [8]. Therefore, the rapid hemostasis, sufficient neovascularization, and effective antimicrobial properties of the wound microenvironment may be critical for the treatment of the difficult-to-heal infectious wounds [9,10]. The ZnO has been widely shown to induce antibacterial effects due to an electrostatic interaction between positively-charged Zn ions (Zn^{2+}) and negatively-charged bacterial cell wall alongside an excessive production of ROS [11,12]. Moreover, ZnO can also induce the rapid homeostasis through protein kinase C (PKC) pathway, which may enhance platelet activity and aggregation [13]. Nevertheless, directly applied ZnO NPs may be easily diffused away from the transplantation site, thereby elevating the pH and inducing potential cytotoxicity. In addition, lack of a stable application form and poor water solubility of ZnO may further impede the application of ZnO NPs for skin repair. Therefore an appropriate carrier material is required to harness ZnO-mediated therapeutic benefits for skin tissue engineering (TE) [14,15].

Electrospinning is a promising micro/nanofabrication method, which may enable the fabrication of ECM-mimetic scaffolds with sufficient porosity and pore diameter. Electrospun scaffolds have already been exploited for drug delivery and tissue engineering (TE) applications [16]. Meanwhile, fibrous membranes may isolate the wound site from the external environment and ensure permeability for the diffusion of oxygen and transport of nutrients [17]. Consequently, the encapsulation of ZnO NPs into ECM-mimetic fibrous scaffolds may help extend their applicability for wound healing applications [18]. We and other researchers have previously fabricated poly(L-lactide-co-glycolide)/-silk-based fibers containing ZnO NPs [14]. Moreover, we have exploited ZnO NPs in conjunction with the other bioactive cues, including glucagon-like peptide-1 (GLP-1) analogue 'liraglutide' [4]. While these studies have unveiled the potential antimicrobial effects of ZnO NPs against Gram-positive (G^+) and Gram-negative (G^-) bacterial species, it yet remains to be elucidated if ZnO NPs may also simultaneously promote hemostatic ability and neo-tissue regeneration. Similarly, while in our previous studies we primarily focused on the antimicrobial properties of ZnO NPs containing dressings, we did not assessed their potential in an infected wound model [19]. The overarching goal of this research was therefore to elucidate multifunctional benefits for skin tissue regeneration, including hemostatic, antibacterial, and angiogenic effects *in vitro* and *S. aureus*-infected wounds in a rat model *in vivo*.

Briefly, we fabricated electrospun membranes containing ZnO NPs and elucidated their potential to promote hemostasis and skin repair in a full-thickness *S. aureus*-infected wound model *in vivo* [19,20]. We deciphered hemostatic, antibacterial and angiogenic effects of ZnO NPs-encapsulated membranes. We further evaluated the membranes for structural analysis, cytocompatibility, antibacterial effect, and hemostatic properties. We also discerned the hemostatic properties of membranes in a rat tail-amputation model and an ear artery injury model in rabbits. Membranes were next subcutaneously implanted for the preliminary biocompatibility. Different types of dressings, such as biocellulose-based dressings (positive control) and ZnO NPs-encapsulated membranes were next transplanted into *S. aureus* infected full-thickness excisional defects. The repaired skin was evaluated for wound closure, neovascularization, and residual bacteria at day 7 after the implantation of membranes. *In vitro* and *in vitro* assays showed that the ZnO NPs may induce infectious skin repair owing to their multiple beneficial aspects, including rapid hemostatic ability, anti-bacterial properties, and improved angiogenesis.

2. Experimental

2.1. Materials

Poly(L-lactide-co-glycolide) (PLGA, L-lactide: Glycolide = 75:25, M_W = 70–110 kDa) was purchased from Jinan Daigang Bioengineering Co., Ltd. (Jinan, China). Gelatin (Gel, Type B, 48722-500G-F) was from the porcine skin and acquired from MP Biomedicals, LLC (Shanghai, China). The ZnO-NPs (size ≤40 nm) were obtained from Sigma Aldrich (Shanghai, China). Tert-butanol was purchased from Sinopharm Chemical Reagent Co., Ltd (Shanghai, China). The 1,1,1,3,3,3-hexafluoro-2-propanol (HFIP) was purchased from Shanghai Darui Fine Chemical Co., Ltd (Shanghai, China). Bacterial species, including *E. coli* (ATCC 25922) and *S. aureus* (ATCC 25923) were received as a gift from the Chinese Academy of Sciences (CAS, Shanghai, China). The NIH-3T3 fibroblasts and human umbilical vein endothelial cells (HUVECs) were purchased from the Typical Culture Collection Committee Cell Bank, CAS (Shanghai, China). Fetal bovine serum (FBS, BC-SE-FBS01) was purchased from BioChannel Biotechnology (Nanjing, China) and the Dulbecco's Modified Eagle's Medium (DMEM, high-sugar complete medium, catalog # 11995) was obtained from Beijing Solarbio Science & Technology Co., Ltd. (Beijing, China). Biocellulose-based wound dressings (Nanoderm; National Arms Approval # 20172640268) were purchased from Shandong Namet Biotechnology Co., Ltd (Jinan, China). All other chemicals were of analytical grade and used without any further purification.

2.2. Preparation of membranes

2.2.1. Preparation of spinning solution

To prepare spinning solution, PLGA and Gel (7:3, w/w) were dissolved in HFIP to afford 10 wt% PLGA/Gel solution (the identification code was PG) [19]. Thereafter, different content of ZnO-NPs (e.g., 1.0, 2.0, 3.0 mg, etc.) were added into a total 10 mL of the PG solution. The solutions containing 1.0, 2.0, and 3.0 mg of ZnO-NPs were indicated as PG@Z1, PG@Z2, and PG@Z3, respectively (Fig. S1).

2.2.2. Preparation of membranes

Fibrous membranes were fabricated by electrospinning (Yongkang Leye Technology Development Co., Ltd. SS-3556H, Beijing, China) with the conditions as follows: Needle size, 21G; applied voltage, 10 kV; flow rate, 1.5 mL/h; collector speed, 200 rotations per minute (rpm); and distance between the spinneret-to-collector, 10 cm. The spinning time for all of the membranes was approximately 3.5 h. Experiments were performed at room temperature (rt, ~25 °C) and a relative humidity was in the range of 45–50%. Membranes were cross-linked with glutaraldehyde (GA) vapors for up to 30 min and stored at 4 °C for the subsequent use.

2.3. Physicochemical characterization

2.3.1. Morphological analysis

Morphological analysis of membranes as well as elemental mapping

(*e.g.,* C, O, N, Zn, etc.) were carried out by scanning electron microscopy (SEM, Hitachi, TM-1000, Tokyo, Japan) with an EDX spectrometer after gold coating (10 mA, 45 s). The average distribution of fibers ($n = 100$) based on the 5 area of a 1500X SEM picture was performed by Image J software (National Institutes of Health, v1.8.0, USA). The PG@Z1 membranes were also analyzed by the TEM (JEM-2100, JEOL, Japan). The XRD (X-Ray Diffraction) was performed in the range of $2\theta = 5°–50°$ (D8 ADVANCE, Bruker, Germany).

2.3.2. The pore size distribution of scaffolds

The pore size distribution of the membranes was investigated by using a CFP-1100-AI capillary flow porometer (PMI Porous Materials Inc., Ithaca, NY, USA). The specimens (thickness = 0.30–0.35 mm and diameter = 30 mm) were punched from PG@Z1 membranes.

2.3.3. The pH of scaffolds after immersion into the PBS in vitro

Membranes ($n = 4$) were weighed (*ca*. 400 mg) and immersed into a centrifuge tube containing 30 mL of phosphate-buffered saline (PBS, pH = 7.28 ± 0.01) and incubated at 37 °C and 120 rpm for up to 1 week. The pH of the solution was measured by using a digital pH meter (PHS3E, Leici, Shanghai, China).

2.3.4. The porosity of scaffolds

The total porosity (P) of scaffolds was measured by using a liquid displacement method [21]. Samples ($n = 5$) were prepared into rectangular shapes (20 mm × 20 mm × 0.3 mm) and weighed (B_0). Afterwards, scaffolds were transferred into absolute ethanol for up to 6 h and then placed on the filter paper to remove the residual ethanol. The weight of the scaffolds was recorded as B_1. The porosity of scaffolds was determined by Eq. (1):

$$P = \frac{(B_1 - B_0)}{(\rho \times V)} \times 100\% \quad (1)$$

Where B_0 and B_1 represent the weight of the scaffolds before and after immersion in the ethanol, respectively, ρ represents the density of the ethanol at rt, and V indicates the volume of the wet scaffolds.

2.3.5. The water absorption capability of scaffolds

Membranes ($n = 3$) were weighed (A_0) and immersed in deionized (DI) water for up to 10 min. Wet samples were placed on a paper towel to drain off the excess water and samples were weighed again (A_x). The water absorption capacity of the membranes was calculated by Eq. (2):

$$\text{Water absorption capacity} = \frac{(A_x - A_0)}{A_0} \times 100\% \quad (2)$$

2.3.6. Mechanical testing

Mechanical properties of membranes ($n = 4$) were measured by uniaxial tensile testing (Instron 5567, USA) by using 200 N load cell. Samples (30 mm × 10 mm) were punched from membranes and evaluated at a strain rate of 10 mm/min. The representative stress-strain curves were recorded and mechanical properties, including tensile strength (TS), elongation at break (Eb), and Young's modulus were calculated.

2.4. Biocompatibility of membranes

2.4.1. Cytocompatibility of scaffolds

For cell culture, membranes were sterilized by using ultraviolet (UV) light for up to 12 h and subsequently washed with PBS three times. Before cell seeding, the UV-treated membranes were incubated along with the DMEM (high glucose medium) for up to 2 h. The NIH-3T3 fibroblasts (1.4×10^4 cells) were seeded on scaffolds and medium (90% DMEM high-sugar complete medium supplemented with 10% FBS) was changed every other day. Cell-seeded membranes were incubated at 37 °C in an incubator at 5% CO_2 for up to 1, 3, and 5 days.

For cell proliferation, cell-seeded membranes were washed with PBS three times and incubated with the 200 μL of cell counting kit-8 (CCK-8) testing solution (serum-free medium: CCK-8 solution = 1:10, v/v). Samples were incubated at 37 °C for 1 h and 100 μL of the solution was collected and transferred into a 96-well plate to measure the absorbance at 450 nm by using a microplate reader (Thermo Fisher Multiskan FC, Thermo Fisher Scientific, Waltham, MA, USA). At day 5, live/dead staining was also performed and the cell-seeded membranes were observed by a fluorescence microscope (Eclipse TS100, Nikon, Japan).

2.4.2. Hemocompatibility

Hemocompatibility of the membranes was assessed by the hemolysis assay. About 5 mL of fresh blood was collected from New Zealand rabbits and centrifuged at 3000 rpm for 10 min to obtain red blood cells (RBCs). The RBCs pellet was washed with normal saline three times and diluted to afford 2% (v/v) cell suspension. Membranes ($n = 3$, 2 mm × 2 mm) were placed into a new tube and 1-mL of RBCs suspension was added. Tubes were incubated at 37 °C for up to 2 h. Thereafter, the cell suspension was collected from each tube and centrifuged at 3000 rpm for up to 10 min. The supernatant was collected and the optical density (OD) was measured at 540 nm. The DI water and normal saline served as positive and negative controls, respectively. Hemolysis ratio was calculated by Eq. (3):

$$\text{Hemolysis ratio } (\%) = \frac{C_T - C_N}{C_P - C_N} \times 100\% \quad (3)$$

The C_T indicates the OD of the sample, while C_P and C_N represent the OD values of positive and negative control groups, respectively.

2.4.3. Blood clotting in vitro

Hemostatic ability of scaffolds was also measured by whole-blood clotting assay *in vitro* [22]. Circular-shaped scaffolds (diameter = 8 mm) were pre-warmed at 37 °C for 30 min. 10% sodium citrate supplemented whole blood (ca. 100 μL) was added onto scaffolds and incubated at 37 °C and 50 rpm. Samples were washed with DI water (ca. 10 mL) to remove unbound cells and incubated in a shaker at 37 °C and 50 rpm for 5 min to collect free erythrocytes ($n = 4$). Recalcified whole-blood diluted with 10 mL of DI water served as a positive control, while normal saline was used as a negative control. The OD values of solutions as well as both types of controls were measured at 540 nm. The blood clotting index (BCI) was calculated by Eq. (4):

$$\text{BCI } (\%) = \frac{(D_T - D_D)}{(D_P - D_D)} \times 100\% \quad (4)$$

where D_T, D_p, and D_D indicate the OD values of the sample, positive control, and negative control, respectively.

The morphological analysis of blood-seeded scaffolds was performed by SEM (Hitachi TM-1000, Japan).

2.4.4. Adhesion of erythrocytes and platelets with fibrous membranes in vitro

Adhesion of erythrocytes and platelets with the membranes was also ascertained. Scaffolds (diameter = 8 mm) were immersed in PBS for 1 h at 37 °C. A drop of anti-coagulated erythrocytes (supplemented with 10% sodium citrate) was added to the samples and incubated at 37 °C for 5 min. Erythrocytes-seeded scaffolds were immersed into DI water to get the solution. The number of adsorbed red blood cells was quantified by measuring the absorbance of the solution at 540 nm.

Platelet-rich plasma (PRP) was obtained by centrifuging the whole blood at 100 × *g* for 10 min. Then, 1 mL of PRP was dropped onto the surface of samples and they were incubated at 37 °C for 1 h. Each sample was washed with PBS to remove non-adhered erythrocytes or platelets. Then, the platelets-seeded scaffolds were rinsed with PBS, fixed with 4% paraformaldehyde (PFA) and stored at 4 °C for 4 h. Scaffolds were dehydrated with the graded ethanol series and sputter-coated with gold

for 45 s at 15 kV. The dried samples were observed by SEM (TM-1000, Hitachi, Tokyo, Japan).

2.4.5. Transwell migration assay in vitro

The migration of HUVECs was studied *in vitro* by using a Transwell migration assay as reported previously with slight modification [23]. Sterilized scaffolds were placed into the bottom of plate and immersed into 500 μL of serum-free medium for 2 h. Cell suspension (ca. 300 μL; 2 × 10^4 cell per insert) was added into the inserts; the latter were placed into the cell culture plate along with medium and incubated at 37 °C with 5 % CO_2 for 12 h. Inserts were washed with PBS and cells were fixed by using 4% PFA (ca. 500 μL) for 20 min and permeabilized with the cold methanol (100%) for 20 min. Then, 500 μL of crystal violet solution was added into the inserts and wells and the plate was incubated for 15 min. Crystal violet was removed from the wells, and the upper part of the inserts was carefully wiped with a cotton-tipped swab. Cells were observed by using an optical microscope (Eclipse TS100, Nikon, Japan).

2.4.6. Scratch wound healing assay

A scratch wound healing assay was performed to evaluate the effect of ZnO on cell migration *in vitro* [24]. The conditioned medium was collected by soaking membranes (10 mm × 10 mm; thickness = 0.30–0.35 mm) in 5 mL of 1% FBS-supplemented low-serum medium for up to 24 h. HUVECs (4 × 10^4 cells) were seeded into 24-well plates and cultured for up to 24 h to afford a confluent cell monolayer. A scratch of approximately 160 μm width was created on the confluent cell monolayer by using a 200 μL pipette tip and the scratched cells were gently washed away with the PBS two times. About 2 mL of low-serum conditioned medium was added into each well. Cells were cultured for up to 24 h and imaged by using an optical microscope (TS100, Nikon, Japan). Images of the migrated cells were collected at $t = 0$ and $t = 24$ h by using an optical microscope (Eclipse TS100, Nikon, Japan). Quantitative analysis was performed to measure initial scratch (E_0) and healed scratch (E_1) areas by using Image J (NIH, v1.8.0, USA). The migration ratio was determined by Eq. (5):

$$\text{Migration ratio} = \left(1 - \frac{E_1}{E_0}\right) \times 100\% \quad (5)$$

Where E_0 and E_1 represented the wound area at $t = 0$ and $t = 24$.

2.4.7. Antibacterial activity

Antibacterial properties of membranes were evaluated by using $Gram^+$ *S. aureus* and $Gram^-$ *E. coli* bacterial species. Membranes ($n = 3$, 15 mm × 15 mm) were sterilized by UV irradiation for up to 12 h. Both types of bacterial species were transferred to bacterial cell culture medium (LB Broth, LB Broth Agar, Sangon Biotech, Shanghai, China) for up to 12 h and incubated at 37 °C to afford a bacterial concentration of 10^5 CFU/mL. About 1 mL of the bacterial culture solution was evenly spread on membranes and incubated at 37 °C for 24 h. All of the bacterial culture solution was transferred to 10 mL of PBS. After dilution, bacterial culture solution (10^3 colony forming units per mL (CFU/mL)) was obtained and evenly spread on an agar plate and incubated at 37 °C for 24 h. The bacteria-seeded membranes were photographed. Pure bacterial suspension without membranes was used as a control group, and the log reduction was calculated by Eq. (6):

$$\text{Log reduction} = \log_{10}\left(\frac{F_1}{F_0}\right) \quad (6)$$

where F_1 and F_0 indicate the number of viable microorganisms in the control group and in the PG, PG@Z1, PG@Z2, and PG@Z3 groups, respectively.

2.5. Animal experiments

Animal experiments were approved by the Institutional Animal Care and Use Committee (IACUC) of the Army Military Medical University, Chongqing, China (AMUWEC20235046).

2.5.1. Subcutaneous implantation of membranes

For preliminary biocompatibility, fibrous membranes were subcutaneously implanted in Sprague-Dawley (SD) rats. Animals were anesthetized by an intraperitoneal injection of 10 wt% chloral hydrate (300 mg kg^{-1}). Dorsal areas of the rats were shaved and disinfected with 70% ethanol. The four pockets were created by the incision of the midline in each rat and the membranes (including PG, PG@Z1, PG@Z2, and PG@Z3; 5 mm × 5 mm; thickness = 0.15 mm) were inserted into the subcutaneous space, and the skin was closed with four stitches (5-0 silk suture). At day 14 and 21, animals were sacrificed with an overdose of chloral hydrate and membranes along with their adjacent tissues were explanted. Main organs, including heart, liver, spleen, lung, and kidney were also obtained at day 21. Explants were fixed with 4% PFA, paraffin-embedded, and sectioned into 5 μm slices. Main organs were stained by hematoxylin and eosin (H&E) while explanted membranes were subjected to H&E staining, Masson's trichrome (MT) staining, and CD31 immunostaining.

2.5.2. Hemostasis studies in vivo

Hemostatic performance of the membranes was evaluated by using a rat tail-amputation model and a rabbit ear artery injury model. For rat tail-amputation model, SD rats ($n = 18$, $n = 3$ per group, weight, 130–200 g) were amputated from tail and randomly divided into 6 groups to either receive gauze (control group, 2 layers, 3 cm × 3 cm) or membranes (3 cm × 3 cm; thickness = ca. 0.35 mm). Membrane groups included PG, PG@Z1, PG@Z2, and PG@Z3. Animals were anesthetized by 10 wt% chloral hydrate solution (300 mg kg^{-1}). A surgical cutting tool was used to cut 50% length of tail, followed by leaving the tail in the air for up to 5 s to ascertain normal blood loss. Next, samples were used to evaluate hemostasis time and blood loss for all groups.

For ear artery trauma model, New Zealand white rabbits (weight = 2 kg and age = 4 weeks) were randomly divided into 6 groups ($n = 3$ for each group). Rabbits were anesthetized by injecting 10 wt% chloral hydrate solution (300 mg kg^{-1}) and were later fixed on an operating table. For an ear artery injury model, the ear skin was shaved and sterilized to expose the artery. Then, 50% of the circumference of the artery on the outer side of the ear was transected carefully to initiate the bleeding, and samples were immediately applied onto the bleeding site with slight pressure.

2.5.3. Infectious wound healing in vivo

Antibacterial properties of electrospun membranes were assessed in an infection model of rat skin by following a previous report [25]. Thirty-six male SD rats (weight = 190–210 g; age = 6 weeks) were randomly divided into six groups: (1) untreated, control group, (2) PG, (3) PG@Z1, (4) PG@Z2, (5) PG@Z3, and (6) biocellulose-based dressings (positive control). All rats were anesthetized by an intraperitoneal injection of 10 wt% chloral hydrate (300 mg kg^{-1}). The skin was shaved and full-thickness excisional defects (diameter = 10 mm) were created on the dorsal side of the animals. About 20 μL of *S.* aureus suspension (10^7 CFU in sterile PBS) was applied to each wound. Membranes were transplanted and replaced every three days to prevent tissue adhesion. Digital images of wounds were captured at day 0, 3, 7, 10, and 14 for all groups. The wound length and wound areas were analyzed by tracing the wound margins and calculated by using Image J (National Institutes of Health, v1.8.0, USA). The wound closure rate was expressed as a percentage area of the original wound area and calculated by Eq. (7) ($n = 5$):

$$\text{Wound closure rate } (\%) = \left(1 - \frac{G_t}{G_0}\right) \times 100\% \quad (7)$$

where G_0 and G_t represent the wound areasat day 0 and at designated

time intervals, respectively.

The bacterial activity was assayed for each group at day 7 post-implantation. Dressings were removed from the wounds and the 300 μL of sterile PBS was added on the wound site. The PBS at the wound site was absorbed by using the cotton guaze. The cotton gauze were immersed into 10 mL of LB liquid medium. A total 100 μL of the solution was seeded on Mueller-Hinton broth at 37 °C overnight to observe the colony growth.

2.5.4. Recovery of biological function

The recovery of the biological function of the skin is an important consideration for wound healing applications. Biomechanical performance of the membranes is one of the important indicators for assessing the biological functional recovery of the repaired skin. The skin was shaved and full-thickness excisional defects (10 mm × 30 mm) were created on the dorsal side of the animals. About 20 μL of *S. aureus* suspension (10^7 CFU in sterile PBS) was introduced. Membranes, including PG, PG@Z1, PG@Z2, and PG@Z3 alongside the P-control were transplanted.

At day 14, repaired skin tissues as well as surrounding tissues were collected and animals were sacrificed with an overdose of the anesthesia. The repaired skin (20 mm × 30 mm) was collected for biomechanical assessment. The explanted skin samples ($n = 6$) were trimmed to 10 mm width and the thickness was measured by using a Vernier caliper. Mechanical properties were measured by a universal mechanical instrument (Instron 5966, USA) at a strain rate of 5 mm/min for up to the rupture of the skin. The failure force (N) and tensile strain (%) were calculated by the software (Bluehill Universal, Norwood, MA, US). The tensile strength (MPa) was calculated from the strain-stress curve. The native skin without an injury was used as a normal group.

2.5.5. Histological analysis

At pre-determined time points, the wounds along with their surrounding tissues were harvested, rinsed in PBS, and fixed in 4% PFA immediately for 24 h at rt. Then tissues were embedded in paraffin and sectioned into 5 μm thick slices. Sections were counter-stained with hematoxylin and eosin (H&E) and Masson's trichrome (MT) staining. The granulation formation was assessed as an average thickness of the dermis. Image J software was used to quantify the numbers of positive cells or positive areas in each field of view.

2.6. Statistical analysis

All data were collected from three independent samples and quantitative data was expressed as mean ± standard deviation (SD). The statistical analysis was performed by using one-way analysis of variance (ANOVA) followed by Tukey's multiple comparison test and the criteria for statistical significance were $^*p < 0.05$, $^{**}p < 0.01$, $^{***}p < 0.001$.

3. Results

3.1. Preparation and characterizations of electrospun scaffolds

The ZnO NPs were encapsulated into PLGA/Gel (PG) fibers by using electrospinning, and the morphology of membranes was discerned by the SEM (Fig. 1a). The fibers exhibited smooth surface morphology. A few fibers encapsulating ZnO NPs showed the formation of beads and agglomerates, thereby displaying a rough surface morphology and a protruded-like structure (Fig. 1a). The EDS mapping displayed a uniform dispersion of carbon (C), oxygen (O), nitrogen (N), and zinc (Zn), which further illustrated that the ZnO NPs can be successfully loaded into electrospun membranes (Fig. 1b). The average diameter of the fibers was 0.49 ± 0.09 μm, 0.61 ± 0.15 μm, 0.61 ± 0.08 μm, and 0.67 ± 0.14 μm for PG, PG@Z1, PG@Z2, and PG@Z3 membranes, respectively (Fig. 1c). The TEM micrograph also showed an encapsulation of ZnO NPs into the fibers (Fig. 2a). The structural analysis of ZnO NPs was further performed by XRD. The ZnO NPs exhibited sharp diffraction peaks at $2\theta = 31.77°$, 34.43°, and 36.25° (Fig. 2b). On the other hand, PG membranes did not exhibit aforementioned diffraction peaks. The PG@Z1 exhibited a weak diffraction peak, thereby indicating the successful incorporation

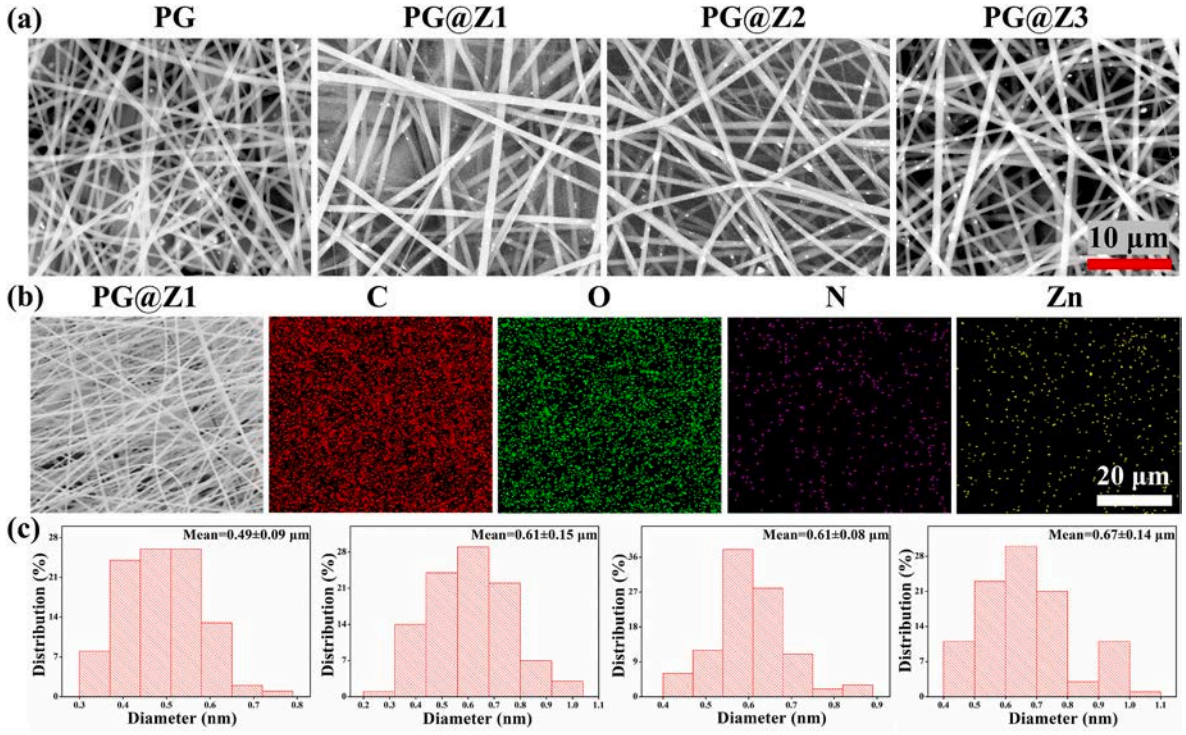

Fig. 1. Morphological analysis of electrospun fibers. (a) SEM micrographs of different types of membranes. Scale bar, 10 μm. (b) EDS analysis of PG@Z1 membrane. Scale bar, 20 μm. (c) Average distribution of fiber diameter.

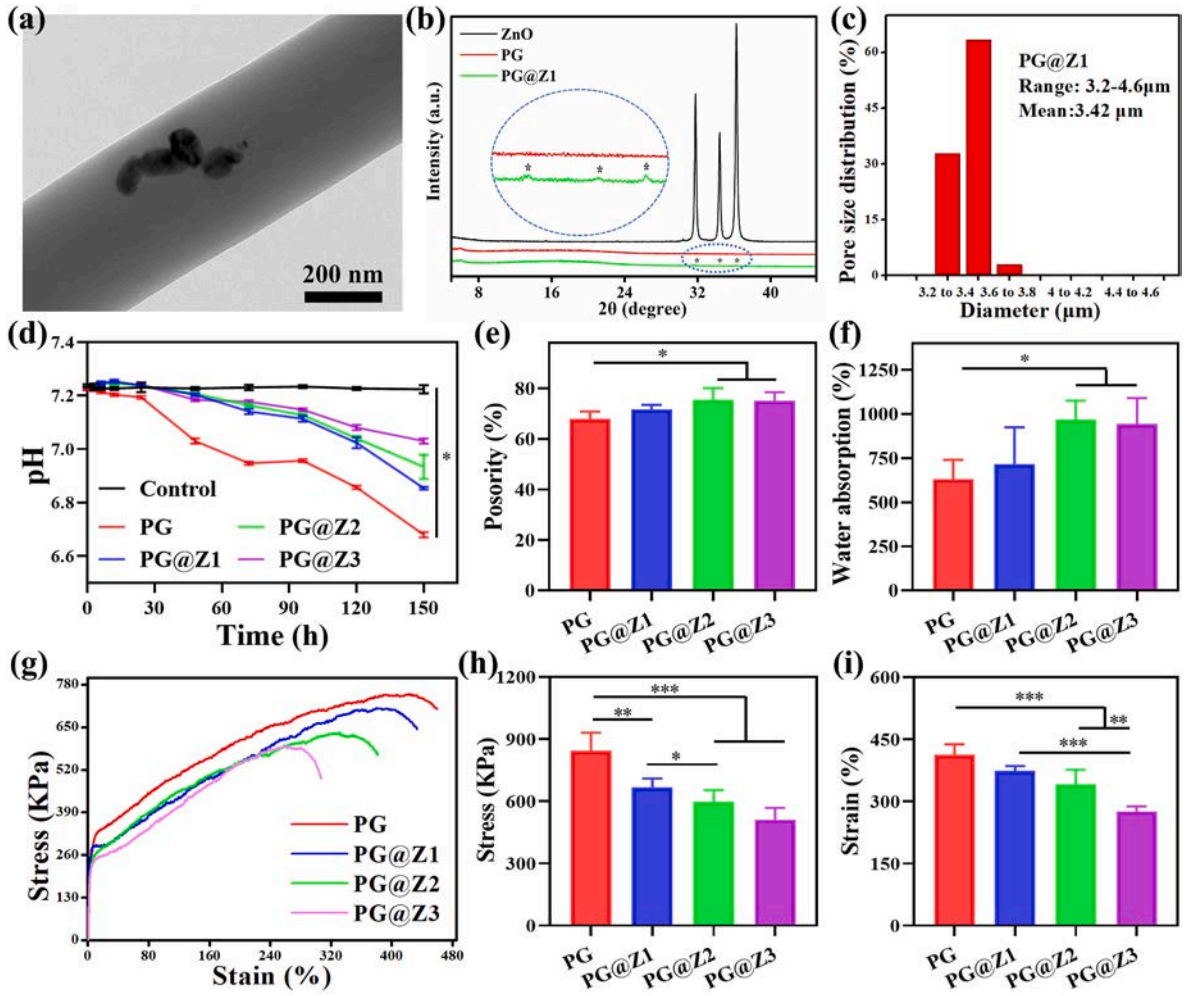

Fig. 2. Characterization of the scaffolds. (a) TEM micrograph of PG@Z1 fibers. Scale bar, 200 nm. (b) XRD spectra of ZnO NPs, PG, and PG@Z1. (c) Pore size distribution of PG@Z1. (d) The cumulative pH of the solution after the immersion of different types of scaffolds in the PBS. The porosity (e), water absorption (f), representative strain-stress curves (g), tensile stress (h), and tensile strain (i) of membranes. $^{*}p < 0.05$, $^{**}p < 0.01$, and $^{***}p < 0.001$.

of ZnO NPs into fibers (Fig. 2b). The porosity and pore size play a pivotal role for the diffusion of oxygen and the transport of nutrients. The pore size distribution of the scaffolds was in the range of 3.2–4.6 μm (Fig. 2c). All of the fibers exhibited sufficient porosity (Fig. 2e, e.g., PG = 68.0 ± 2.9%; PG@Z1 = 71.8 ± 1.7%; PG@Z2 = 75.5 ± 4.6%; and PG@Z3 = 75.2 ± 3.4%).

Membranes were immersed into PBS and the pH values of the solution were measured for up to different time points. The pH values of PG, PG@Z1, PG@Z2, and PG@Z3 groups were evaluated to be 7.2 ± 0.2, 6.7 ± 0.0, 6.9 ± 0.0, 6.9 ± 0.1, and 7.0 ± 0.0, respectively at 150 h (Fig. 2d). As can be noticed from these values, there was an insignificant difference among groups in terms of the pH. Since electrospun membranes should exhibit sufficient water uptake, which may play an important role to absorb the wound exudate, we further examined the water uptake by the membranes. All membranes showed rapid water absorption (PG = 631.9 ± 108.7%; PG@Z1 = 717.1 ± 207.2%; PG@Z2 = 968.2 ± 106.7%; and PG@Z3 = 943.3 ± 146.8%) at 6 min (Fig. 2f). The good moisture uptake of the membranes may also have implications for the rapid blood uptake for coagulation function during the earlier stages of wound repair.

Wound dressings with appropriate mechanical properties may be beneficial for maintaining the integrity of the scaffolds as well as supporting the cell adhesion [1]. We assessed the tensile mechanical properties of scaffolds. Representative stress-strain curves showed that the membranes obeyed the Hooke's law in the initial stage followed by the plastic deformation beyond the yield point (Fig. 2g). The membranes showed a decreasing trend in the tensile stress and tensile strain with an increase in the content of ZnO NPs. The values of the tensile stress were 843.0 ± 88.2 kPa, 667.5 ± 41.8 kPa, 597.5 ± 55.5 kPa, and 511.3 ± 57.8 kPa, while for the tensile strain were 413.3 ± 24.8%, 373.8 ± 11.9%, 341.3 ± 35.1%, and 276.5 ± 11.9% for PG, PG@Z1, PG@Z2, and PG@Z3 membranes, respectively (Fig. 2h–i). Nonetheless, the membranes containing ZnO NPs display reasonable mechanical properties to serve as bandages for skin regeneration as it has been reported previously [21].

3.2. Cytocompatibility and blood compatibility of membranes

The cytocompatibility of membranes was discerned by seeding NIH-3T3 fibroblasts on membranes followed by the live/dead staining and CCK-8 assay. Cells survived well on the scaffolds and virtually no dead cells could be observed in all groups at day 5 (Fig. 3a). The CCK-8 assay showed a concomitant increase in the cell proliferation over time (Fig. 3e).

Since wound dressings directly interact with the wound bed and blood, hemostatic ability of scaffolds was examined [20]. All of the membranes displayed negligible hemolysis and exhibited hemolysis ratio values lower than that of the 2% (PG = 0.63 ± 0.28%; PG@Z1 = 0.72 ± 0.30%; PG@Z2 = 0.92 ± 0.30%; and PG@Z3 = 1.33 ± 0.28%) (Fig. 3f). The supernatants obtained from the different types of

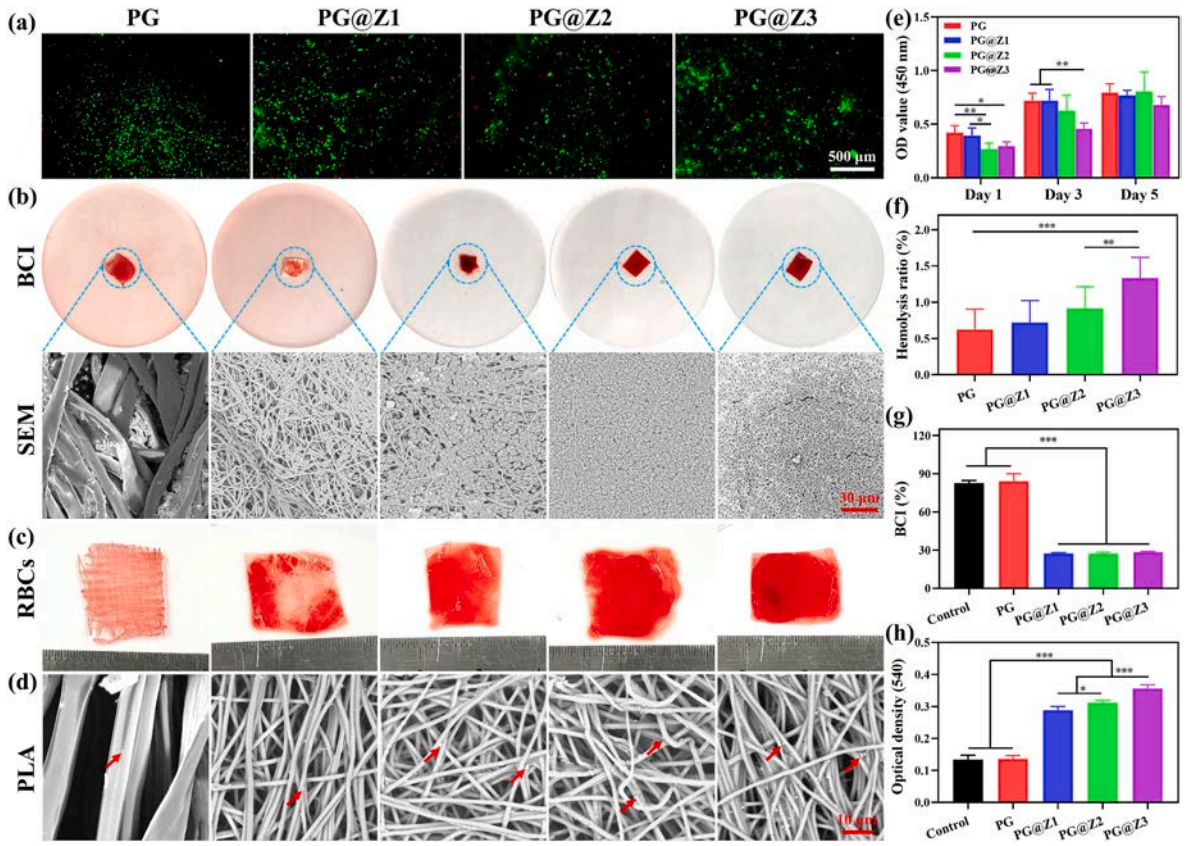

Fig. 3. Cytocompatibility and hemocompatibility of electrospun fibers containing ZnO NPs. Live/dead staining of cell-seeded membranes at day 5 (a). Blood clotting assay (b). Coagulation assay by using erythrocytes (c). SEM micrographs of membranes after coagulation with the PRP (d). CCK-8 assay (e), hemolysis ratio (f), BCI (g), and OD values of erythrocytes-seeded scaffolds (h) at 540 nm $*p < 0.05$, $**p < 0.01$, and $***p < 0.001$.

membranes displayed slightly yellowish colour after hemolysis assay, which replicated the negative control while differed from the positive control (bright red colour) (See Fig. S2 of Supporting Information). These data indicated good hemostatic ability of membranes, which was also well-below the international standard of 5%) [26].

3.3. Biological functions of membranes in vitro

The hemostatic properties of membranes were further examined by measuring BCI, erythrocytes, and platelets adhesion *in vitro*. As shown in Fig. 3b, membranes containing ZnO NPs exhibited excessive residual blood clots as compared to the other groups. The control and PG groups showed an obvious increase in the color of the water due to hemolysis. Morphological analysis by SEM showed an adhesion of sufficiently more number of erythrocytes in the membrane containing ZnO NPs, which indicated that the incorporation of ZnO NPs may be conducive to promote hemostasis for blood clotting (Fig. 3b). The BCI values were found to be 82.8 ± 2.0, 84.3 ± 5.8, 27.5 ± 0.6, 27.4 ± 1.0, and 28.5 ± 0.6 for control, PG, PG@Z1, PG@Z2, and PG@Z3 groups, respectively (Fig. 3g). The blood coagulation was also examined by seeding erythrocytes on the different types of membranes and OD values were measured (Fig. 3c). The membranes containing ZnO NPs led to the significant adhesion of erythrocytes than that of the control and PG membranes (Fig. 3h; control = 0.13 ± 0.01; PG = 0.14 ± 0.01; PG@Z1 = 0.29 ± 0.01; PG@Z2 = 0.31 ± 0.01; and PG@Z3 = 0.36 ± 0.01). Moreover, fibers containing ZnO NPs induced markedly higher platelet adhesion than that of the control and PG groups (Fig. 3d).

The migration of HUVECs towards different types of membranes was assessed by a Transwell migration assay, which also revealed a distinct chemotactic effect of ZnO NPs on cell recruitment. The number of migrated HUVECs were significantly higher in the membranes containing ZnO NPs than that of the control and PG groups (Fig. 4a & 4d; control = 8.7 ± 1.0; PG = 29.5 ± 1.2; PG@Z1 = 68.7 ± 0.6; PG@Z2 = 82.0 ± 2.9, and PG@Z3 = 75.3 ± 2.5 per HPF (high power field)). In addition, a scratch wound healing assay was performed to discern the effect of the ZnO NPs on cell migration *in vitro*. While exhibiting a similar initial wound depth, the conditioned medium obtained from the membranes containing ZnO NPs showed distinctly higher migration of HUVECs at 24 h (Fig. 4b). The cell migration ratio was found to be 34.1 ± 3.6%, 36.0 ± 4.7%, 78.5 ± 6.0%, 76.5 ± 2.3%, and 69.1 ± 7.9% for control, PG, PG@Z1, PG@Z2, and PG@Z3 membranes, respectively (Fig. 4e).

Antibacterial properties of membranes were assessed by using *E. coli* and *S. aureus*. Membranes containing ZnO NPs significantly suppressed the survival of both types of bacterial species (Fig. 4c). For *E.* coli, the values for the log reduction were 0.05 ± 0.02, 0.94 ± 0.02, 1.16 ± 0.03, 1.19 ± 0.01 for PG, PG@Z1, PG@Z2, and PG@Z3, respectively (Fig. 4f). On the other hands, for *S. aureus*, these values were 0.06 ± 0.03, 1.10 ± 0.03, 1.12 ± 0.05, 1.27 ± 0.07 for PG, PG@Z1, PG@Z2, and PG@Z3, respectively (Fig. 4g). Anti-bacterial activity of membranes did not obviously vary with an increase in the content of ZnO NPs. Nevertheless, membranes containing ZnO NPs showed significantly higher antibacterial effect against *S. aureus* and *E. coli in vitro*.

3.4. Subcutaneous implantation of membranes

The preliminary biocompatibility of fibrous membranes was evaluated by subcutaneous implantation in rats for up to 14 and 21 days. The H&E staining displayed an intensive cell infiltration into the membrane at day 14 and 21 both from the muscle and skin sides, while the implanted scaffolds were accompanied by a color change from the heavy pink of the less cellular inner part to the light pink of the heavily

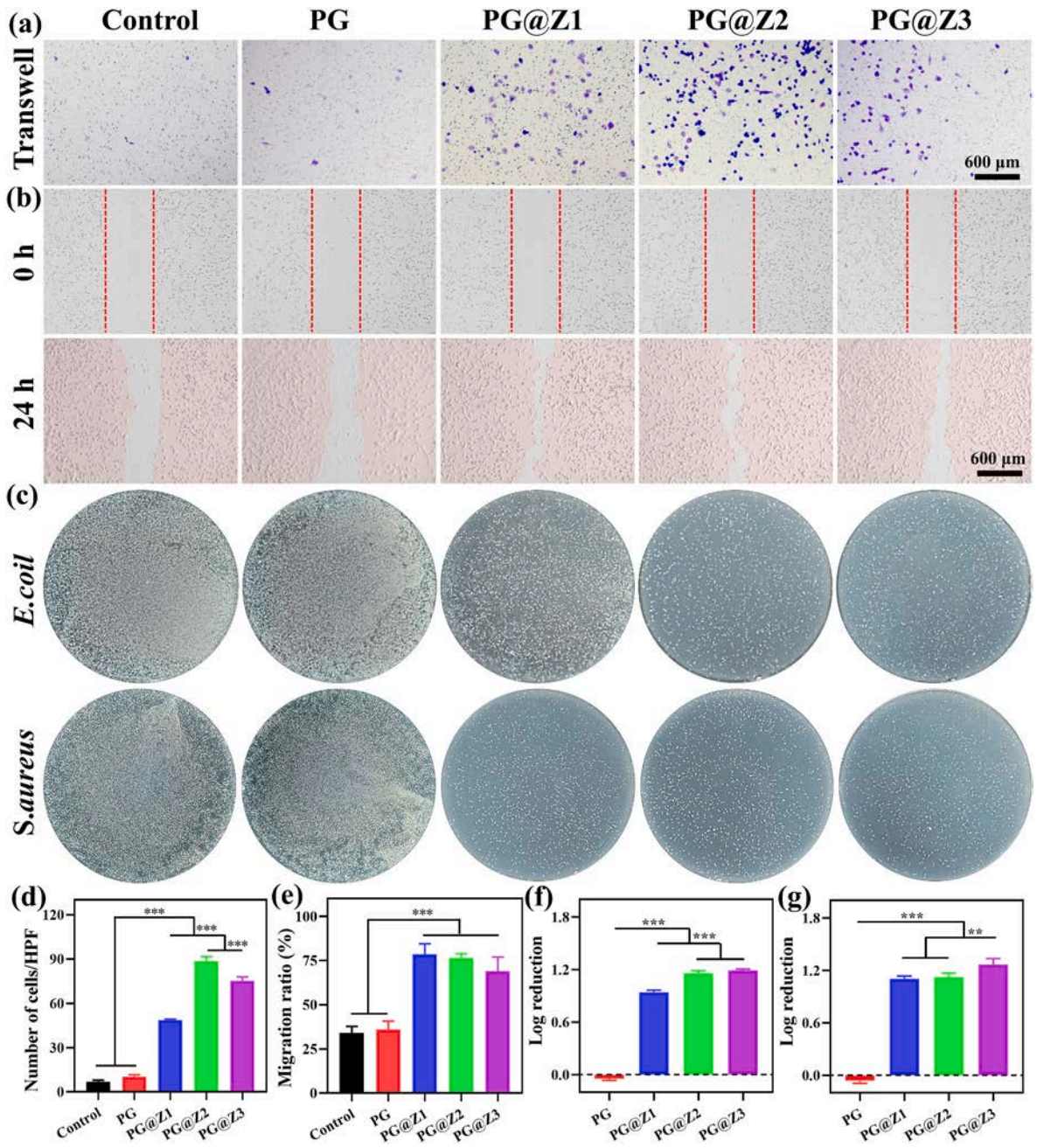

Fig. 4. Transwell migration assay and antibacterial properties of membranes. Transwell migration assay at 12 h (a) and migration of HUVECs in a scratch wound healing assay at 0 and 24 h (b). Scale bar = 600 μm and applies to all of the images. (c) Survival of *E.* coli (upper panel) and *S.* aureus (lower panel) on broth agar plates after treatment with different types of scaffolds. Quantitative analysis of the migration ratio of HUVECs in a Transwell migration assay (d) and a scratch wound healing assay (e). The log decrease of *E. coli* (f) and *S. aureus* (g) treated with the different types of scaffolds. $^{*}p < 0.05$, $^{**}p < 0.01$, and $^{***}p < 0.001$.

infiltrated cellular areas over time (Fig. 5a). Masson's trichrome staining revealed an accumulation of collagenous tissues (Fig. 5b). Membranes loaded with ZnO NPs exhibited residual scaffolds (please see red pentagrams in the images) than that of the PG group by day 21, which may be ascribed to an incomplete degradation of ZnO NPs (Fig. 5b). The CD31 staining of explanted scaffolds showed the presence of $CD31^{+}$ endothelial cells (ECs) in all groups at day 14, which were mainly localized in the groups loaded with the ZnO NPs (Fig. 5c). On the other hand, the PG group showed only a few numbers of $CD31^{+}$ ECs by day 21. These data showed that the ZnO NPs may induce neo-vessel formation *in vivo* (Fig. 5c).

Altogether, these results revealed that the membranes had good biocompatibility; infiltrated cells as well as ECM may promote tissue repair. Histomorphometric analysis of main organs, such as heart, liver, spleen, lung, and kidney did not reveal an obvious cytotoxicity, which further corroborated cytocompatibility results (Fig. 5d).

3.5. Hemostatic properties of membranes in vivo

Based on the good biocompatibility and blood coagulation of membranes *in vitro*, hemostatic properties of scaffolds were further assessed in a rat tail-amputation model and a rabbit ear artery injury model (Fig. 6b) [22]. Blood loss and hemostatic time were used as parameters to access the hemostatic properties. In a rat tail-amputation model, the fibrous scaffolds loaded with ZnO NPs showed good hemostatic ability in term of blood loss and hemostatic time as compared to the PG and

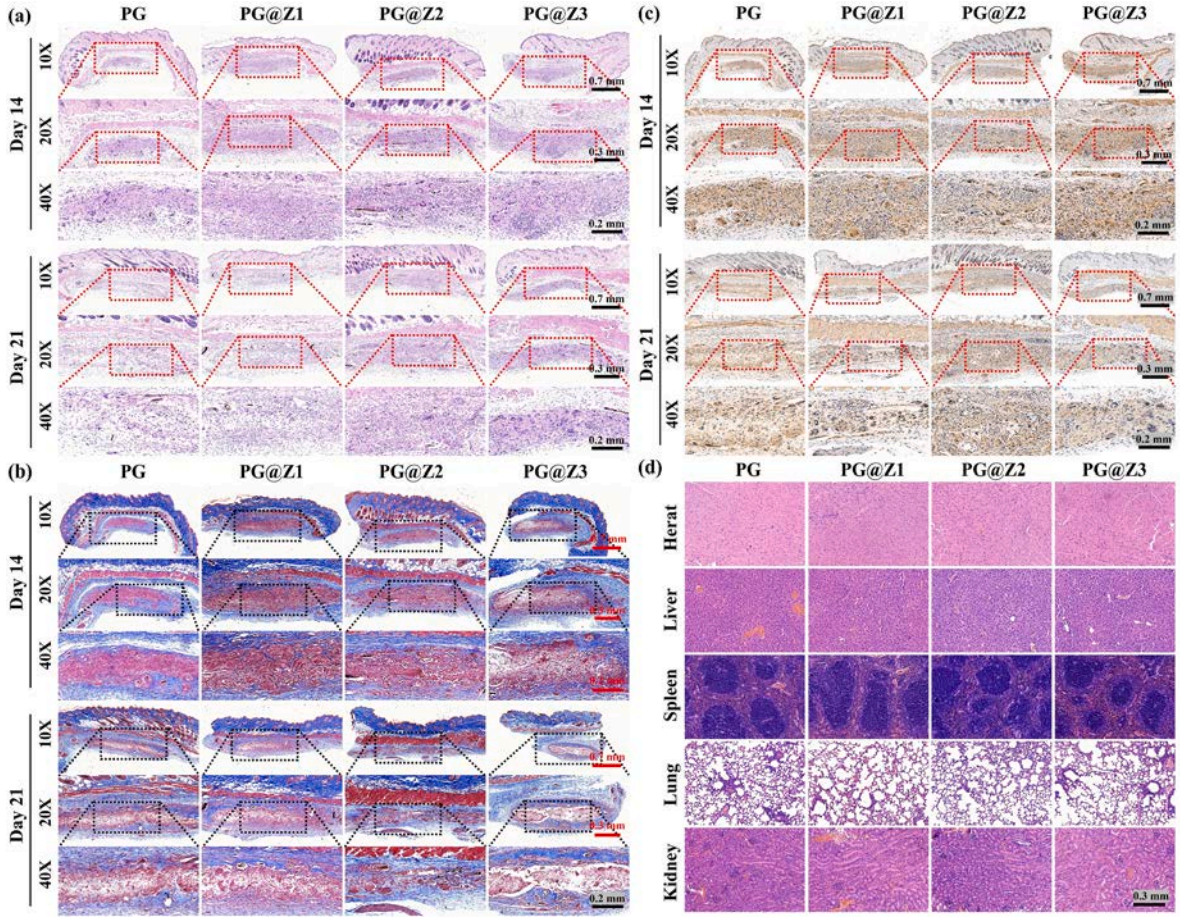

Fig. 5. Subcutaneous implantation of membranes for up to 14 and 21 days. H&E staining (a) and Masson's trichrome staining (b). The CD31 immunostaining (c). Scale bars: 0.7 mm, 0.3 mm, and 0.2 mm. (g) H&E staining of main organs collected from rats transplanted with fibrous membranes for up to 21 days (g). Scar bar: 0.3 mm.

control groups (Fig. 6a, 6c–d; blood loss: control = 102.6 ± 8.4 mg; PG = 41.7 ± 4.4 mg; PG@Z1 = 10.7 ± 0.7 mg; PG@Z2 = 9.8 ± 1.7 mg; and PG@Z3 = 8.1 ± 0.6 mg and hemostatic time: control = 54.3 ± 4.1 s, PG = 49.0 ± 1.8s; PG@Z1 = 22.0 ± 2.6 s; PG@Z2 = 19.5 ± 2.4 s; and PG@Z3 = 14.8 ± 2.5 s). The fibrous membranes containing ZnO NPs also displayed higher hemostatic ability (e.g., short hemostatic time, <20 s), a high hemostatic efficiency, less blood loss, and a smaller blood stain size than that of the control and PG groups in an ear artery injury model of rabbits (Fig. S3, Supporting Information).

3.6. Wound healing in vivo

Membranes were next evaluated in a *S. aureus*-infected full-thickness excisional defect model in rats (Fig. 7a) [23]. Wounds in all groups were photographed and the wound closure rate was measured by using image J. Wounds in all groups had gradually healed and only a small wound area was left 14 days post-operatively (Fig. 7c). Wounds treated with PG@Z1, PG@Z2, and PG@Z3 membranes exhibited rapid healing and fast recovery than that of the other groups at day 10 and 14 (Fig. 7e). The wounds in the control group were also rapidly healed, which may be ascribed to the self-healing ability of the rats. Nevertheless, wound healing in the control group was very slow as compared to the other groups. The wound closure rate was found to be 83.6 ± 1.0%, 91.3 ± 0.9%, 95.5 ± 2.4%, 97.2 ± 0.7%, 96.9 ± 0.4%, and 95.2 ± 1.3% for control, PG, PG@Z1, PG@Z2, PG@Z3 membranes, and P-Control group, respectively by day 14 (Fig. 7f). The fast wound healing in the PG@Z2 and PG@Z3 groups may be ascribed to ZnO NPs. It is worthy to note that the P-Control group also did not show an appreciable advantage in term of tissue repair than that of the membranes containing ZnO NPs (Fig. 7c).

To further evaluate the amount of the residual bacteria in the wound environment, we used a spread plate method [27]. The wound exudate collected at day 7 post-operatively was grown on Mueller-Hinton broth (Fig. 7b). The control and PG groups lacked antibacterial activity and yielded bacterial colonies similar to the *S. aureus*-infected wounds. In contrast, PG@Z2 and PG@Z3 groups induced the significant reduction of the bacterial colonies. The percentage values of the survived bacteria were 100.0 ± 3.5%, 106.9 ± 7.3%, 61.2 ± 6.3%, 21.2 ± 3.7%, and 10.1 ± 3.1% for control, PG, PG@Z1, PG@Z2, and PG@Z3 membranes, respectively. These results showed good antibacterial effect of PG@Z2 and PG@Z3 membranes (Fig. 7g).

H&E staining of the explanted wounds showed non-healed full-thickness skin defects accompanied by a large number of inflammatory cells in the wound center and margin by the day 7 (Fig. 8a). The epithelial layer was not completely regenerated in control, PG group, and P-Control groups. In contrast, re-epithelialization was sufficiently increased in the wounds treated with the membranes containing ZnO NPs. Epithelium thickness was evaluated to be 37.9 ± 15.2 μm, 59.2 ± 9.7 μm, and 55.2 ± 8.5 μm for PG@Z1, PG@Z2, and PG@Z3 membranes, respectively by day 14 (Fig. 8d). By day 14, membranes containing ZnO NPs also showed less scar tissue formation than that of the control, PG groups, and P-control group (Fig. 8e; scar length, control = 2.19 ± 0.12 mm; PG = 2.34 ± 0.19 mm; PG@Z1 = 1.83 ± 0.19 mm; PG@Z2 = 53 ± 0.16 mm; PG@Z3 = 1.77 ± 0.20 mm; P-Control = 1.91 ± 0.11 mm). Therefore, both the PG@Z2 and PG@Z3 groups exhibited rapid wound closure accompanied by the less wound length, which may

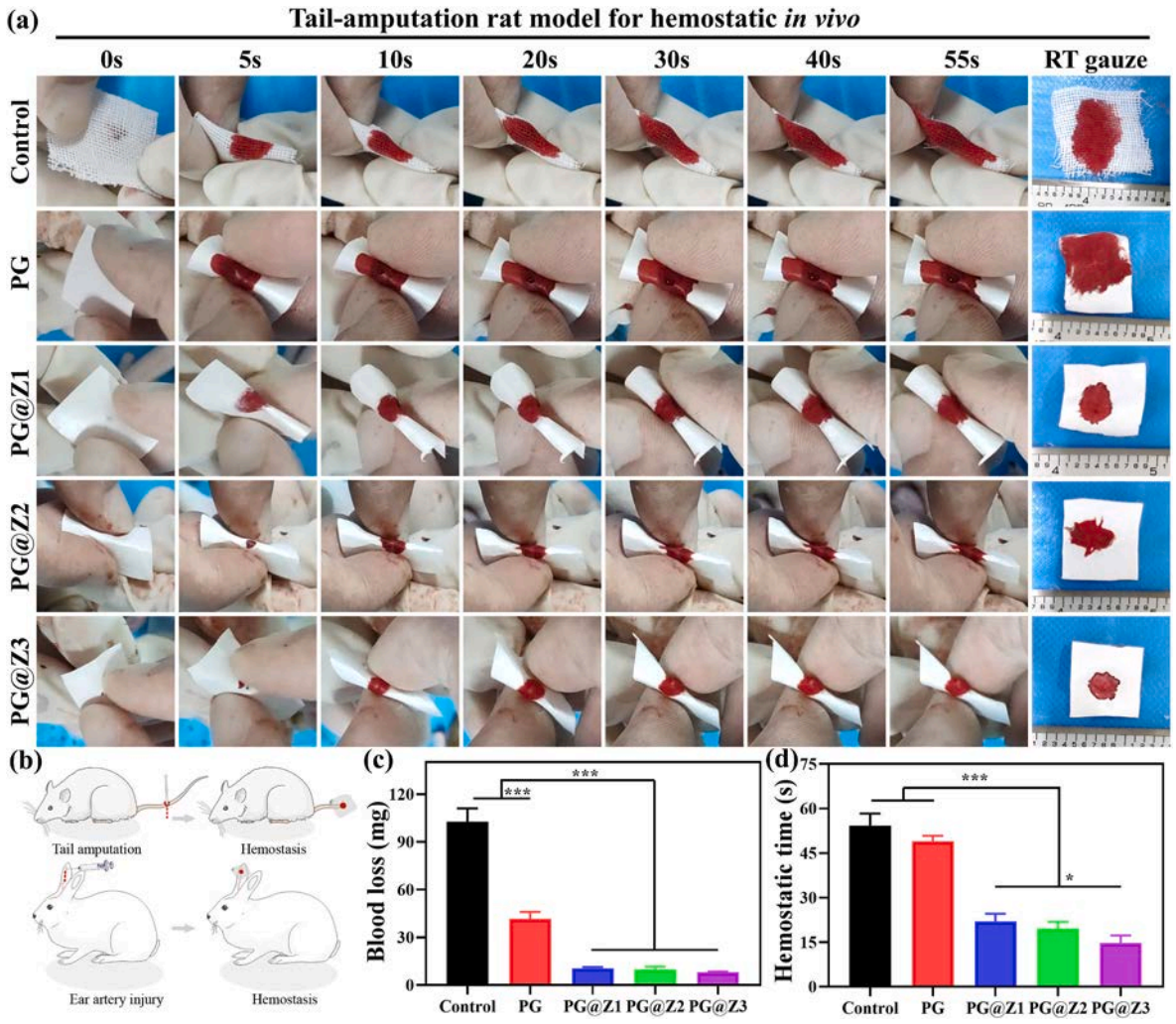

Fig. 6. Hemostatic properties of fibrous membranes in a rat tail-amputation model *in vivo*. (a) Photographs showing the treatment of the tail amputation with the different types of membranes for up to 0, 5, 10, 20, 30, 40, 55 s after injury. (b) Schematic illustration of hemostasis process in different models. Quantitative analysis of blood loss (c) and hemostatic time (d). $*p < 0.05$, $**p < 0.01$, and $***p < 0.001$.

be attributable to the ZnO NPs. The MT staining also showed the deposition and maturation of collagen within the healed wounds. By day 14, PG@Z2 and PG@Z3 treated wounds also displayed the deposition of ECM along with well-organized fibroblasts (Fig. 8b). It is worthy to note that by the day 14, wounds treated with the PG@Z1 and PG@Z2 showed morphology similar to that of the normal skin and did not show an accumulation of inflammatory cells (Fig. S4, Supporting Information). Interestingly, the control, PG, and P-Control groups did not contain antibacterial substances, resulting in slow tissue regeneration and repair, incomplete regeneration of the epithelial layer, and a large number of inflammatory cells remaining in the center of the wound (Fig. 8a–b).

To evaluate the functional recovery of the regenerated skin, mechanical properties were measured at day 14 post-operatively (Fig. 8c); native skin served as the normal group [28]. The representative stress-strain curves exhibited an initial stiffening behavior followed by the yield and fracture in all groups (Fig. 8f). The values for failure force were 6.66 ± 2.17 N, 7.83 ± 0.83 N, 9.29 ± 1.68 N, 9.96 ± 1.25 N, 10.1 ± 1.6 N, 6.97 ± 1.10 N, and 13.1 ± 1.50 N for control, PG, PG@Z1, PG@Z2, and PG@Z3, P-Control, and normal groups, respectively (Fig. 8g). Ultimate tensile strength (UTS) was found to be 0.74 ± 0.11 MPa, 0.58 ± 0.06 MPa, 0.81 ± 0.18 MPa, 0.82 ± 0.13 MPa, 0.86 ± 0.18 MPa, 1.02 ± 0.14 MPa, and 1.15 ± 0.15 MPa for control, PG, PG@Z1, PG@Z2, and PG@Z3, P-Control, and normal groups, respectively (Fig. S5a, Supporting Information). On the other hand, *Eb* (%) was found to be 70.8 ± 15.9%, 61.8 ± 9.9%, 110.8 ± 14.0%, 111.4 ± 6.7%, 118.0 ± 4.7%, 125.40 ± 13.16%, and 130.6 ± 9.6% for control, PG, PG@Z1, PG@Z2, and PG@Z3, P-Control, and normal groups, respectively (Fig. S5b, Supporting Information). As can be observed from these data, the PG@Z2 and PG@Z3 groups showed significantly higher UTS as compared to the other groups. The improved tensile properties of the regenerated skin can be ascribed to the beneficial effects of ZnO NPs, which can suppress bacterial growth, promote vascular regeneration and collagen deposition, thereby accelerating the restoration of normal skin functions. It is worthy to note that the mechanical parameters of the PG@Z2 and PG@Z3 groups did not reach for up to the level of the normal group; the ECM components and cellular tissues are well-organized in the latter which may have only partially regenerated with the application of wound dressings. By day 14, the regenerated wounds manifested epithelial regeneration and collagen remodeling. The regeneration of the other components may require further implantation period [6].

4. Discussion

The chronic skin injuries display poor healing due to dysregulated homeostasis, persistent pathogen infection, an excessive production of peroxides, prolonged inflammation, and poor angiogenesis. This leads to

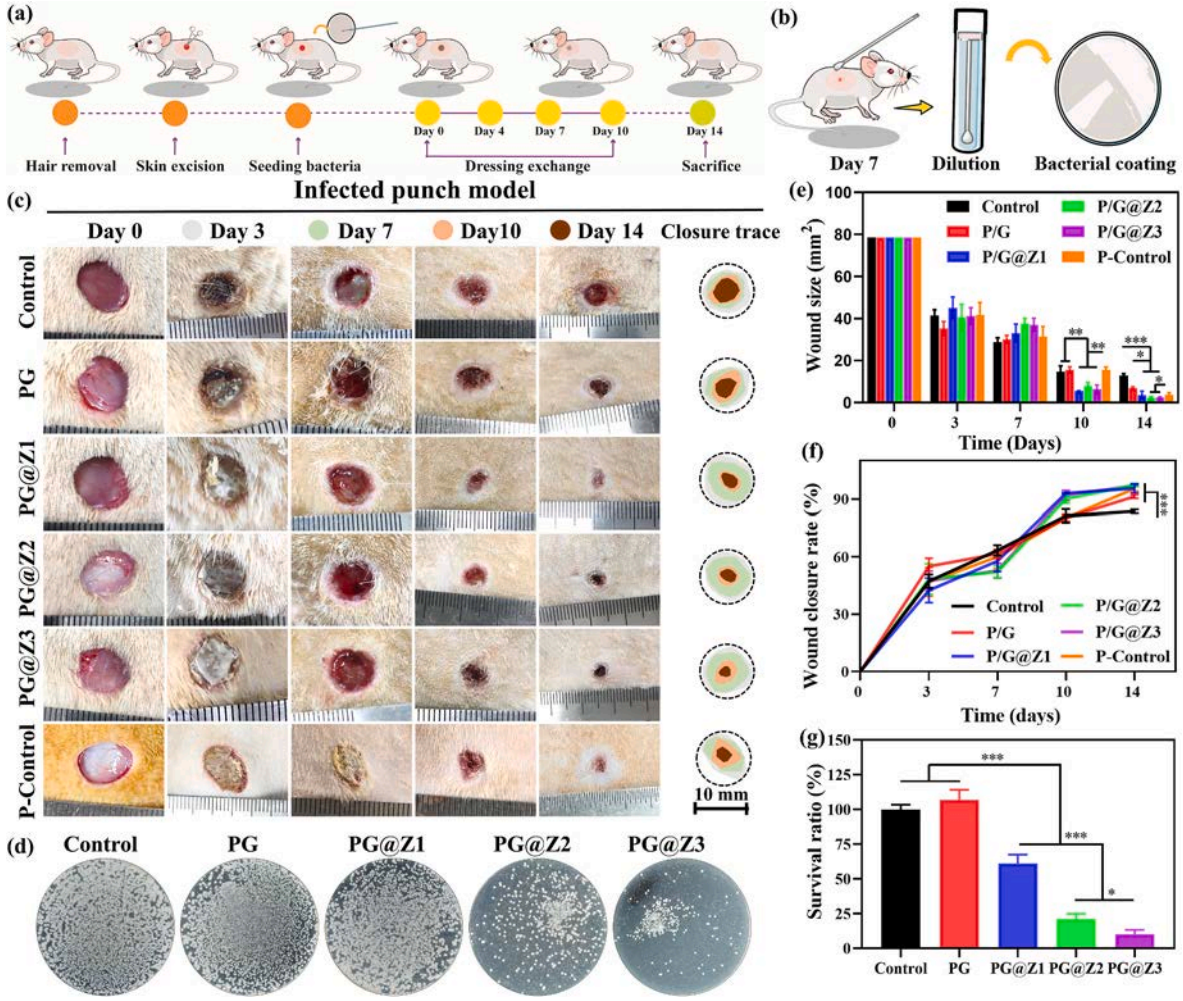

Fig. 7. Evaluation of membranes for skin repair in a full-thickness excisional defect model in *S. aureus* infected rats. (a) Schematic diagram of the implantation of membranes. (b) Antibacterial assessment of the wounds (b). Untreated wounds and bacterial cellulose membranes were used as controls and positive group, respectively. (c) Representative images of wound area and closure trace of wounds by day 14. Scale bar, 10 mm. (d) Growth of *E.coil* collected from various wound exudates at day 7. (e) Wound area at each time point normalized with respect to day 0. (f) Percentage wound closure rate at day 14. (g) Survival ratio of residual bacteria at wound site by day 7. $*p < 0.05$, $**p < 0.01$, and $***p < 0.001$.

an impaired healing response as well as an exacerbated inflammatory response, which necessitate alternative curative approaches [29]. Since wound healing is a considerably dynamic process, the performance requirements of the wound dressings should be modified with the healing progress [30]. Thus, an ideal wound dressing should not only leverage a moist and a breathable environment, but should also display homeostasis, anti-bacterial, anti-oxidative, and anti-inflammatory properties as well as promote tissue regeneration [31,32]. Therefore, innovative scaffolds which can facilitate the multiple aspects of wound healing may hold great promise for skin regeneration.

Different types of inorganic NPs, including silver (Ag) and copper oxide (CuO) possess good antibacterial properties and have garnered considerable attention of the research community for the management of infected tissue injuries [33]. Nevertheless, certain risks, including the potential toxicity of NPs hamper their clinical translatability [34]. We and other researchers have alternatively exploited ZnO NPs as antibacterial agents, which have shown significant promise for soft and hard tissue repair [35]. The distinct advantages of ZnO NPs involve good bactericidal properties, angiogenic hemostatic ability, and anti-oxidative potential [36]. In addition to its antibacterial properties, ZnO may also play a pivotal role for wound healing (Fig. 9).

Gauze and cotton wool are generally used as wound dressings. However, the pain caused by their removal alongside a sluggish regenerative response may hamper their applicability. Alternative wound dressings, including hydrogels and electrospun fibers have been harnessed owing to their tunable porosity, morphology, and anti-oxidative capabilities [37]. In addition, hydrogels and electrospun fibers are advantageous owing to their abilities to confer a moist wound environment, good adaptability for wound bed while minimal adhesion with the host tissues and pain relief due to a cooling effect. Nevertheless, these hydrogels and fibers still need additional components to confer them with the multifunctional characteristics, such as antibacterial activity, angiogenic ability, and scarless tissue repair. We exploited electrospun fibers, thanks to their good porosity and adaptability for patching the soft tissue [38]. Structural and morphological analysis by using a battery of assays revealed successful incorporation of ZnO NPs into fibers as well as their homogenous distribution in dressings as revealed by EDS analysis (Fig. 1b). PLGA and Gel were employed as components for dressings due to their fast degradation and good hydrophilicity, respectively [39]. Moreover, ZnO NPs encapsulated dressings showed a porous structure and a rapid water uptake, which may have implications for the uptake of wound exudate and the regulation of the humidity at injury site (Fig. 2f) [40]. The dressings also supported good cell viability and growth while exhibited lower hemolysis ratio, which reflect their good biocompatibility (Fig. 3f). Since bacterial infections at the injury site could perturb and delay the wound

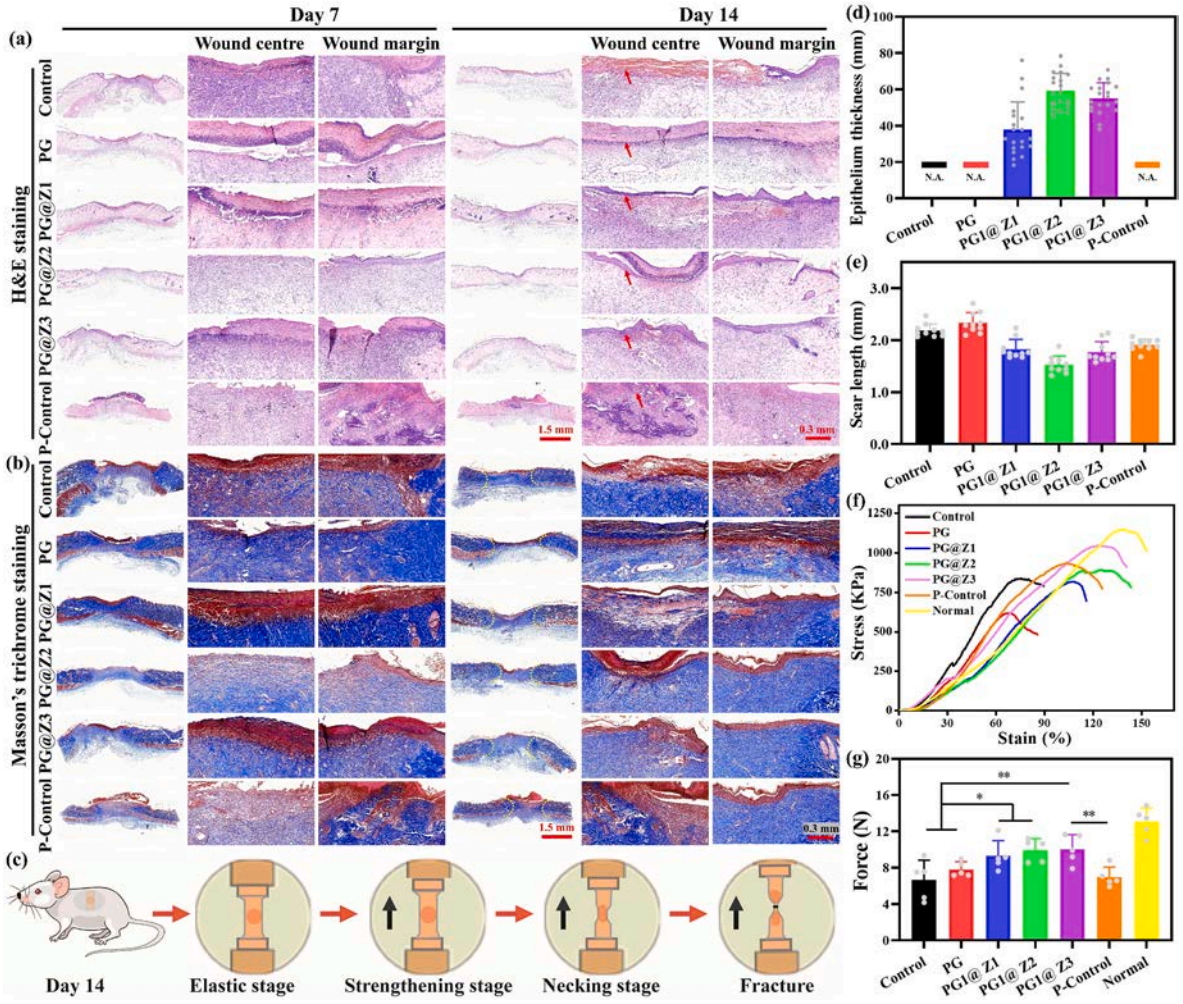

Fig. 8. Histological analysis of repaired skin. H&E staining (a) and Masson's trichrome staining of wound center and margins at day 7 and 14. (c) Schematic diagram showing analysis of regeneration skin tissues for mechanical properties. Epithelium thickness (d) and scar length (e). Representative tensile stress-strain curves (f) and failure force (g) of the repaired skin in various groups at day 14. $*p < 0.05$, $**p < 0.01$, and $***p < 0.001$.

healing process, we exploited *S.* aureus and *E.* coli to discern antibacterial properties of membranes [31,41]. Electrospun membranes encapsulating ZnO NPs efficiently inhibited the activity of the *S. aureus* and *E. coli*. The improved antibacterial activity of ZnO NPs loaded dressings may be ascribed to the release of zinc ions (Zn^{2+}), which may directly interact with the negatively-charged bacterial membranes as well as increase the permeability of bacterial cell membranes, thereby triggering bacterial cell death [11,30]. Moreover, ZnO NPs may physically adhere to bacterial cell wall to induce cell apoptosis and phospholipid peroxidation; ROS and hydroxyl free radicals (OH·) may further exacerbate bactericidal effects [42,43]. It is worthy to note that further in-depth studies are still required to clearly elucidate the ZnO NPs mediated antibacterial effects.

Good hemostatic properties of dressings may help manage fast wound healing after injury. A series of assays, including BCI, adhesion of erythrocytes and platelets assays *in vitro* as well as a rat tail-amputation model and an ear artery injury model in rabbit altogether manifested good hemostatic capabilities of ZnO NPs loaded dressings (Fig. 6a). The good hemostatic ability of membranes may be described as follows: the implantation of ZnO NPs-loaded scaffolds may block the wound sites through wet adhesion due to high water absorption and physical barriers, which may prevent bleeding [22]. Second, the membranes loaded with ZnO NPs may release Zn^{2+}; the latter have been shown to mediate the coagulation pathway and affect hemostasis, plausibly by increasing the phosphorylation of the protein kinase C in platelets, activating intrinsic and extrinsic coagulation pathways, and augmenting platelet activation and aggregation [44]. Third, fibrous membranes may absorb RBCs and platelets and accelerate blood coagulation [3]. When a biomaterial comes in contact with the blood, fibrinogen and other proteins of blood are preferentially adsorbed on the surface of the biomaterial and stimulate platelet adhesion and aggregation, which further result in the activation of clotting events [32]. Thus, cessation of bleeding by ZnO NPs-encapsulated scaffolds may be ascribed to the activation of the intrinsic and extrinsic coagulation pathways as well as rapid clot formation.

The regeneration of skin, as a complex structural and functional organ, also requires further evaluation of mechanical properties, nerve innervation, and scar inhibition [45,46]. Wounds treated with PG@Z2 and PG@Z3 membranes showed good re-epithelialization, neovascularization, granulation tissue formation, and mechanical properties (Fig. 8a–b). Enhanced wound recovery may be ascribed to the ZnO NPs, which may increase cell growth, neovascularization, and collagen production [47,48]. The PG@Z2 and PG@Z3 membranes also showed more numbers of neo-vessels and good mechanical properties of repaired skin. Altogether, ZnO NPs may promote infectious wound healing owing to its multiple effects, including anti-inflammatory and anti-bacterial properties (Fig. 9).

This study has also several limitations. While we have observed significant reduction in the bacterial colonies in the wounds treated with ZnO NPs containing membranes than that of the untreated (control) and

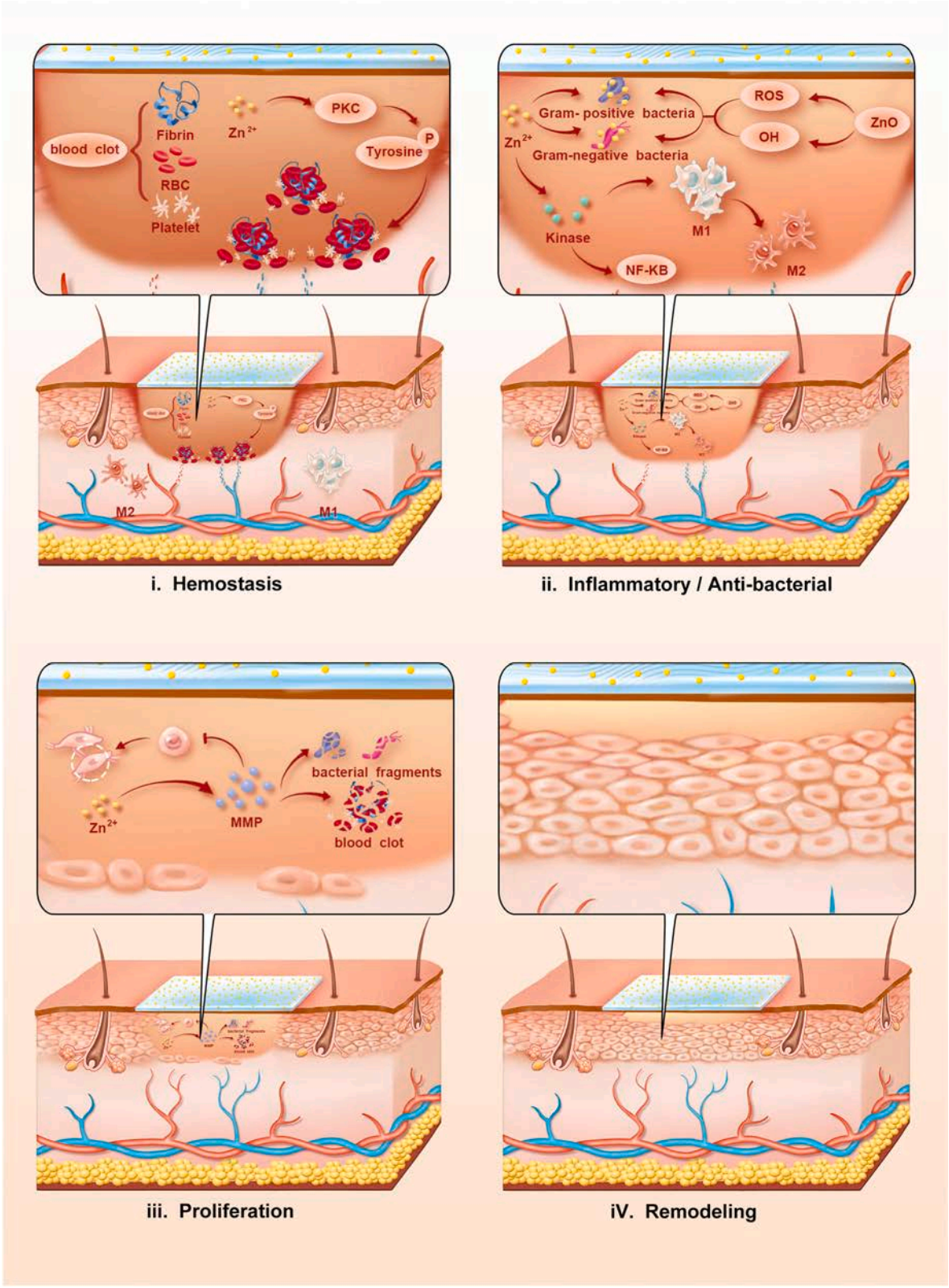

Fig. 9. The illustration of the dynamic and interactive process mechanism of PG@ZnO dressing during wound healing process.

PG (ZnO NPs-free) membranes, we did not clarify the nature of the survived bacteria. Therefore, clear elucidation of the complete profile of the residual bacteria at the wound bed may hold great promise. The use of advanced techniques, such as polymerase chain reaction (PCR) may help further clarify this aspect. Nevertheless, it is worthy to note that the spread plate method has also been previously used by the other researchers to gain an insight into the antimicrobial properties of membranes *in vivo*. Shi et al. studied the survival of *S. aureus* and *P. aeurginosa* *in vivo* and reported cobalt (Co) concentration-mediated antibacterial effect of dressings [51]. Besides, live/dead staining manifested a

reduction in the live bacteria while an increase in the dead bacteria. Similarly, we have used S. *aureus*-infected wound model, which however may not accurately reflect the clinical situations of the infected wounds. Therefore, the use of clinically-relevant bacterial species, such as Pseudomonas aeurginosa (*P.* aeurginosa) may further help clearly elucidate the potential antimicrobial and reparative benefits of membranes. Nevertheless, we have observed multifunctional benefits of ZnO NPs in conjunction with electrospun membranes, such as good hemostatic ability, antimicrobial activity, neo-vessel regeneration, and wound healing (please see Table S1–S7 for statistical analysis of different types of groups for *in vitro* and *in vivo* assays, Supporting Information).

5. Conclusions

In summary, we have successfully prepared electrospun membranes loaded with the ZnO NPs, which have shown rapid hemostatic ability alongside good anti-bacterial effects and anti-oxidative properties. We deciphered structural and morphological properties of dressings as well as carried out a series of *in vitro* experiments, which revealed substantial effect of ZnO-mediated therapeutic ions and bioactive components in leveraging multiple functionalities, such as rapid hemostasis, substantial angiogenesis, diminished bacterial colonization, and anti-oxidant *in vitro*. The assessment of the preliminary biocompatibility of dressings in a subcutaneous implantation model revealed orchestration of membranes with the endogenous cellular components as well as the formation of neo-tissues, thereby revealing the remodeling of membranes *in vivo*. Once transplanted in a full-thickness excisional infectious wound model *in vivo*, composite membranes containing ZnO substantially improved wound re-epithelialization and neo-vessel formation, induced macrophages polarization, suppressed inflammation, and promoted scarless wound healing. Conclusively, our approach of simultaneously harnessing economical ZnO NPs to impart multifunctionality to the fibrous dressings may provide an alternative avenue for scarless wound healing, which may also have implications for the other bio-related disciplines.

Declaration of competing interest

The authors declare that they have no known competing financial interests or personal relationships that could have appeared to influence the work reported in this paper.

Data availability

Data will be made available on request.

Acknowledgements

This work was supported by National Natural Science Foundation of China (81501606), Enhancement of technological innovation capabilities Foundation of Army Military Medical University (2019XYY15). The part of this research was also funded by Donghua University Postgraduate Innovation and Entrepreneurship Ability Training Program (yjssc2023002). This research was also supported by Science and Technology Commission of Shanghai Municipality, China (No. 20S31900900, 20DZ2254900) and Sino German Science Foundation Research Exchange Center, China (M – 0263), China Education Association for International Exchange (2022181). This project was also supported by Researchers Supporting Project Number (RSP2023R65), King Saud University, Riyadh, Saudi Arabia.

Appendix A. Supplementary data

Supplementary data to this article can be found online at https://doi.org/10.1016/j.jddst.2023.105072.

References

[1] Z. Yuan, L. Zhang, S. Jiang, M. Sha, Y. Cai, Y. Chen, J. Song, X. Yu, H. Ijima, Y. Xu, X. Mo, Anti-inflammatory, antibacterial, and antioxidative bioactive glass-based nanofibrous dressing enables scarless wound healing, Smart Mater. Med. 4 (2023) 407–426, https://doi.org/10.1016/j.smaim.2023.01.001.
[2] L. Li, X. Cheng, Q. Huang, Y. Cheng, J. Xiao, J. Hu, Sprayable antibacterial hydrogels by simply mixing of aminoglycoside antibiotics and cellulose nanocrystals for the treatment of infected wounds, Adv. Healthcare Mater. 2201286 (2022), 2201286, https://doi.org/10.1002/adhm.202201286.
[3] S. Wang, H. Zheng, L. Zhou, F. Cheng, Z. Liu, H. Zhang, L. Wang, Q. Zhang, Nanoenzyme-reinforced injectable hydrogel for healing diabetic wounds Infected with Multidrug Resistant Bacteria, Nano Lett. 20 (2020) 5149–5158, https://doi.org/10.1021/acs.nanolett.0c01371.
[4] X. Han, S. Chen, Z. Cai, Y. Zhu, W. Yi, M. Guan, B. Liao, Y. Zhang, J. Shen, W. Cui, D. Bai, A diagnostic and therapeutic hydrogel to promote vascularization via blood sugar reduction for wound healing, Adv. Funct. Mater. 14 (2023), 221308, https://doi.org/10.1002/adfm.202213008.
[5] F. Zou, Y. Wang, T. Tang, Y. Zheng, Y. Xie, S. Zhu, H. Yang, H. Meng, X. Liu, J. Yang, Synergistic strategy constructed hydrogel-aerogel biphase gel (HAB-gel) with self-negative-pressure exudate absorption, M2 macrophage-polarized and antibacterial for chronic wound treatment, Chem. Eng. J. 451 (2023), 138952, https://doi.org/10.1016/j.cej.2022.138952.
[6] H. Zhao, J. Huang, Y. Li, X. Lv, H. Zhou, H. Wang, Y. Xu, C. Wang, J. Wang, Z. Liu, ROS-scavenging hydrogel to promote healing of bacteria infected diabetic wounds, Biomaterials 258 (2020), 120286, https://doi.org/10.1016/j.biomaterials.2020.120286.
[7] Q. Lei, D. He, L. Ding, F. Kong, P. He, J. Huang, J. Guo, C.J. Brinker, G. Luo, W. Zhu, Y. Yu, Microneedle patches integrated with biomineralized melanin nanoparticles for simultaneous skin tumor photothermal therapy and wound healing 2113269 (2022) 1–14, https://doi.org/10.1002/adfm.202113269.
[8] Y. Tomar, N. Pandit, S. Priya, G. Singhvi, Evolving trends in nanofibers for topical delivery of therapeutics in skin disorders, ACS Omega 8 (2023) 18340–18357, https://doi.org/10.1021/acsomega.3c00924.
[9] A.A. Gorustovich, J.A. Roether, A.R. Boccaccini, Effect of bioactive glasses on angiogenesis: a review of in vitro and in vivo evidences, Tissue Eng., Part B 16 (2010) 199–207, https://doi.org/10.1089/ten.teb.2009.0416.
[10] M.T. Noman, N. Amor, M. Petru, Synthesis and applications of ZnO nanostructures (ZONSs): a review, Crit. Rev. Solid State Mater. Sci. 47 (2022) 99–141, https://doi.org/10.1080/10408436.2021.1886041.
[11] S. Jelodari, H. Daemi, P. Mohammadi, J. Verdi, M.J. Al-Awady, J. Ai, M. Azami, Assessment of the efficacy of an LL-37-encapsulated keratin hydrogel for the treatment of full-thickness wounds, ACS Appl. Bio Mater. (2022), https://doi.org/10.1021/acsabm.2c01068.
[12] M.U.A. Khan, W.S. Al-Arjan, N. Ashammakhi, S. Haider, R. Amin, A. Hasan, A. Hasan, Multifunctional bioactive scaffolds from ARX- g-(Zn@rGO)-HAp for bone tissue engineering: in vitro antibacterial, antitumor, and biocompatibility evaluations, ACS Appl. Bio Mater. 5 (2022) 5445–5456, https://doi.org/10.1021/acsabm.2c00777.
[13] J. Ma, C. Wu, Bioactive inorganic particles-based biomaterials for skin tissue engineering, Exploration 2 (2022), 20210083, https://doi.org/10.1002/exp.20210083.
[14] J. Han, Y. Sun, T. Wu, X. Hou, S. Zheng, H. Zhang, T. Lin, H. Liu, T. Sun, Echinacoside-Zinc nanomaterial inhibits skin glycation by suppressing the transcriptional activation of the receptor for advanced glycation end-products, ACS Nano 17 (2023) 14123–14135, https://doi.org/10.1021/acsnano.3c04726.
[15] G. Kaur, G. Narayanan, D. Garg, A. Sachdev, I. Matai, Biomaterials-based regenerative strategies for skin tissue wound healing, ACS Appl. Bio Mater. 5 (2022) 2069–2106, https://doi.org/10.1021/acsabm.2c00035.
[16] S. Mcloughlin, A.R. Mckenna, J.P. Fisher, Fabrication strategies for engineered thin membranous tissues, ACS Appl. Bio Mater. 6 (2023) 2546–2561, https://doi.org/10.1021/acsabm.3c00133.
[17] M. Yu, J. Huang, T. Zhu, J. Lu, J. Liu, X. Li, X. Yan, F. Liu, Liraglutide-loaded PLGA/gelatin electrospun nanofibrous mats promote angiogenesis to accelerate diabetic wound healing via the modulation of miR-29b-3p, Biomater. Sci. (2020) 4225–4238, https://doi.org/10.1039/d0bm00442a.
[18] L. Ma, Y. Sun, Q. Cheng, Z. Yang, J. Wang, Z. Xu, M. Yang, Y. Shuai, Silk protein-mediated biomineralization : from bioinspired strategies and advanced functions to biomedical applications, ACS Appl. Mater. Interfaces 15 (2023) 33191–33206, https://doi.org/10.1021/acsami.3c04067.
[19] F. Wu, Z. Yuan, M. Shafiq, L. Zhang, M. Rafique, F. Yu, M. EL-Newehy, H. EL-Hamshary, Y. Morsi, Y. Xu, X. Mo, Synergistic effect of glucagon-like peptide-1 analogue liraglutide and ZnO on the antibacterial, hemostatic, and wound healing properties of nanofibrous dressings, J. Biosci. Bioeng. 134 (2022) 248–258, https://doi.org/10.1016/j.jbiosc.2022.06.004.
[20] L. Teng, Z. Shao, Q. Bai, X. Zhang, Y.S. He, J. Lu, D. Zou, C. Feng, C.M. Dong, Biomimetic glycopolypeptide hydrogels with tunable adhesion and microporous structure for fast hemostasis and highly efficient wound healing, Adv. Funct. Mater. 31 (2021) 1–11, https://doi.org/10.1002/adfm.202105628.
[21] Y. Chen, Z. Yuan, W. Sun, S. Muhammad, J. Zhu, J. Chen, H. Tang, Vascular endothelial growth factor - recruiting nanofiber bandages promote multifunctional skin regeneration via improved angiogenesis and immunomodulation, Adv. Fiber Mater. 5 (2022) 327–348, https://doi.org/10.1007/s42765-022-00226-8.
[22] Z. Ahmadian, A. Correia, M. Hasany, P. Figueiredo, F. Dobakhti, M.R. Eskandari, S. H. Hosseini, R. Abiri, S. Khorshid, J. Hirvonen, H.A. Santos, M.A. Shahbazi, A hydrogen-bonded extracellular matrix-mimicking bactericidal hydrogel with

radical scavenging and hemostatic function for pH-responsive wound healing acceleration, Adv. Healthcare Mater. 10 (2021) 1–19, https://doi.org/10.1002/adhm.202001122.
[23] Y.M. Gao, Z.Y. Li, X.J. Zhang, J. Zhang, Q.F. Li, S.B. Zhou, One-pot synthesis of bioadhesive double-network hydrogel patch as disposable wound dressing, ACS Appl. Mater. Interfaces 15 (2023) 11496–11506, https://doi.org/10.1021/acsami.2c19931.
[24] S. Li, Z. Li, J. Yang, Y. Ha, X. Zhou, C. He, Inhibition of sympathetic activation by delivering calcium channel blockers from a 3D printed scaffold to promote bone defect repair, Adv. Healthcare Mater. 11 (2022) 1–15, https://doi.org/10.1002/adhm.202200785.
[25] Q. Hou, K. Liu, C. Lian, J. Liu, W. Wei, T. Qiu, H. Dai, A gelatin-based composite hydrogel with a " one stone , two birds " strategy for photothermal antibacterial and vascularization of infected wounds, Biomacromolecules 24 (2023), https://doi.org/10.1021/acs.biomac.3c00471, 3397-3310.
[26] R. Kandi, P.M. Pandey, M. Majood, S. Mohanty, Fabrication and characterization of customized tubular scaffolds for tracheal tissue engineering by using solvent based 3D printing on predefined template, Rapid Prototyp. J. 27 (2021) 421–428, https://doi.org/10.1108/RPJ-08-2020-0186.
[27] X. Shi, Z. Chen, Y. He, Q. Lu, R. Chen, C. Zhao, D. Dong, Y. Sun, H. He, Dual light-responsive cellulose nanofibril-based in situ hydrogel for drug-resistant bacteria infected wound healing, Carbohydr. Polym. 297 (2022), 120042, https://doi.org/10.1016/j.carbpol.2022.120042.
[28] Z. Yuan, D. Sheng, L. Jiang, M. Shafiq, A. ur R. Khan, R. Hashim, Y. Chen, B. Li, X. Xie, J. Chen, Y. Morsi, X. Mo, S. Chen, Vascular endothelial growth factor-capturing aligned electrospun polycaprolactone/gelatin nanofibers promote patellar ligament regeneration, Acta Biomater. 140 (2022) 233–246, https://doi.org/10.1016/j.actbio.2021.11.040.
[29] Q. Zhang, C. Chang, C. Qian, W. Xiao, H. Zhu, J. Guo, Z. Meng, W. Cui, Z. Ge, Photo-crosslinkable amniotic membrane hydrogel for skin defect healing, Acta Biomater. 125 (2021) 197–207, https://doi.org/10.1016/j.actbio.2021.02.043.
[30] A.E. Stoica, C. Chircov, A.M. Grumezescu, Hydrogel dressings for the treatment of burn wounds: an up-to-date overview, Materials 13 (2020) 1–24, https://doi.org/10.3390/ma13122853.
[31] P. Ray, R. Chakraborty, O. Banik, E. Banoth, P. Kumar, Surface engineering of a bioartificial membrane for its application in bioengineering devices, ACS Omega 8 (2022) 3606–3629, https://doi.org/10.1021/acsomega.2c05983.
[32] S. Zhang, J. Ye, X. Liu, G. Wang, Y. Qi, T. Wang, Y. Song, Y. Li, G. Ning, Dual stimuli-responsive smart fibrous membranes for efficient photothermal/photodynamic/chemo-therapy of drug-resistant bacterial infection, Chem. Eng. J. 432 (2021), 134351, https://doi.org/10.1016/j.cej.2021.134351.
[33] B. Yuan, H. Chen, R. Zhao, X. Deng, G. Chen, X. Yang, Z. Xiao, A. Aurora, B.A. Iulia, K. Zhang, X. Zhu, A.V. Iulian, S. Hai, X. Zhang, Construction of a magnesium hydroxide/graphene oxide/hydroxyapatite composite coating on Mg–Ca–Zn–Ag alloy to inhibit bacterial infection and promote bone regeneration, Bioact. Mater. 18 (2022) 354–367, https://doi.org/10.1016/j.bioactmat.2022.02.030.
[34] L. Chen, Y. Guo, L. Chen, K. Hu, L. Ruan, P. Li, X. Cai, B. Li, Q. Shou, G. Jiang, Injectable Zn2+ and paeoniflorin release hydrogel for promoting wound healing, ACS Appl. Bio Mater. 6 (2023) 2184–2195, https://doi.org/10.1021/acsabm.3c00059.
[35] M. Jabli, Synthesis, characterization, and assessment of cationic and anionic dye adsorption performance of functionalized silica immobilized chitosan bio-polymer, Int. J. Biol. Macromol. 153 (2020) 305–316, https://doi.org/10.1016/j.ijbiomac.2020.02.323.
[36] S. Amjadi, H. Almasi, M. Ghorbani, S. Ramazani, Reinforced ZnONPs/rosemary essential oil-incorporated zein electrospun nanofibers by κ-carrageenan, Carbohydr. Polym. 232 (2020), 115800, https://doi.org/10.1016/j.carbpol.2019.115800.
[37] Z. Jia, J. Gong, Y. Zeng, J. Ran, J. Liu, K. Wang, C. Xie, X. Lu, J. Wang, Bioinspired conductive silk microfiber integrated bioelectronic for diagnosis and wound healing in diabetes, Adv. Funct. Mater. 31 (2021) 1–13, https://doi.org/10.1002/adfm.202010461.
[38] Z. Zhou, T. Deng, M. Tao, L. Lin, L. Sun, X. Song, D. Gao, J. Li, Z. Wang, X. Wang, J. Li, Z. Jiang, L. Luo, L. Yang, M. Wu, Snail-inspired AFG/GelMA hydrogel accelerates diabetic wound healing via inflammatory cytokines suppression and macrophage polarization, Biomaterials 299 (2023), 122141, https://doi.org/10.1016/j.biomaterials.2023.122141.
[39] L. Li, R. Hao, J. Qin, J. Song, X. Chen, F. Rao, J. Zhai, Y. Zhao, L. Zhang, J. Xue, Electrospun fibers control drug delivery for tissue regeneration and cancer therapy, Adv. Fiber. Mater. 4 (2022), https://doi.org/10.1007/s42765-022-00198-9, 1475-1413.
[40] R. Stone, E.C. Saathoff, D.A. Larson, J.T. Wall, N.A. Wienandt, S. Magnusson, H. Kjartansson, S. Natesan, R.J. Christy, Accelerated wound closure of deep partial thickness burns with acellular fish skin graft, Int. J. Mol. Sci. 22 (2021) 1–18, https://doi.org/10.3390/ijms22041590.
[41] L. Wang, Z. Zhao, J. Dong, D. Li, W. Dong, H. Li, Y. Zhou, Q. Liu, B. Deng, Mussel-inspired multifunctional hydrogels with adhesive, self-healing, antioxidative, and antibacterial activity for wound healing, ACS Appl. Mater. Interfaces 15 (2023) 16515–16525, https://doi.org/10.1021/acsami.3c01065.
[42] Y. Du, J. Zhang, S. Yan, Z. Tao, C. Wang, M. Huang, X. Zhang, PEGylated zinc oxide nanoparticles induce apoptosis in pancreatic cancer cells through reactive oxygen species, IET Nanobiotechnol. 13 (2019) 80–84, https://doi.org/10.1049/iet-nbt.2018.5327.
[43] Z. Yuan, Y. Zhao, M. Shafiq, J. Song, J. Hou, Y. Liang, X. Yu, Multi - functional fibrous dressings for burn injury treatment with pain and swelling relief and scarless wound healing, Adv. Fiber Mater. (2023), https://doi.org/10.1007/s42765-023-00320-5.
[44] X. Liu, B. Gaihre, L. Li, A. Rezaei, M. Tilton, B.D. Elder, L. Lu, Bioorthogonal "click chemistry" bone cement with bioinspired natural mimicking microstructures for bone repair, ACS Biomater. Sci. Eng. 9 (2023) 1585–1597, https://doi.org/10.1021/acsbiomaterials.2c01482.
[45] Q. Tang, Q. Ke, Q. Chen, X. Zhang, J. Su, C. Ning, L. Fang, Flexible, breathable, and self-powered patch assembled of electrospun polymer triboelectric layers and polypyrrole-coated electrode for infected chronic wound healing, ACS Appl. Mater. Interfaces (2023), https://doi.org/10.1021/acsami.3c00500.
[46] Y. Shen, G. Xu, H. Huang, K. Wang, H. Wang, M. Lang, H. Gao, S. Zhao, Sequential release of small extracellular vesicles from bilayered thiolated alginate/polyethylene glycol diacrylate hydrogels for scarless wound healing, ACS Nano 15 (2021) 6352–6368, https://doi.org/10.1021/acsnano.0c07714.
[47] J. Liu, M. Wu, J. Lu, Q. He, J. Zhang, Janus intelligent antibacterial hydrogel dressings for chronic wound healing in diabetes, ACS Appl. Polym. Mater. 5 (2023) 2596–2606, https://doi.org/10.1021/acsapm.2c02196.
[48] C. Hong, H. Chung, G. Lee, C. Kim, D. Kim, S.J. Oh, S.H. Kim, K. Lee, Hydrogel/nanofiber composite wound dressing optimized for skin layer regeneration through the mechanotransduction-based microcellular environment, ACS Appl. Bio Mater. 6 (2023) 1774–1786, https://doi.org/10.1021/acsabm.3c00014.